Nanoscale processes of trace element mobility in metamorphosed zircon

E. M. Peterman[1]* S. M. Reddy[2,3] D. W. Saxey[2], D. Fougerouse[2,3], D. R. Snoeyenbos[4], W. D. A. Rickard[2]

[1] Earth and Oceanographic Science, Bowdoin College, Brunswick, ME 04011 USA.

[2] Geoscience Atom Probe Facility, Advanced Resource Characterisation Facility, John de Laeter Centre, Curtin University, GPO Box U1987, Perth, WA 6845, Australia.

[3] School of Earth and Planetary Sciences, Curtin University, GPO Box U1987, Perth, WA 6845, Australia.

[4] Department of Geosciences, University of Massachusetts, Amherst, MA 01003 USA.

*epeterma@bowdoin.edu

Keywords:

Zircon
Atom probe tomography
Nanoscale
Interface coupled dissolution reprecipitation
Trace element geochemistry
Metamorphism

Abstract

Several examples of zircon grains from high- to ultrahigh-pressure (*UHP*) and ultrahigh-temperature *(UHT)* metapelites exhibit a characteristic, yet atypical, core-rim interface domain <5 μm wide observed in cathodoluminescence (CL) imaging. The interface domain is located immediately against the magmatic core and is comprised of an irregular, 0–2 μm wide, CL-dark domain that is rimmed by a complex, 0–5 μm wide, CL-bright domain with cuspate margins. The outer margin of the interface domain is rimmed by intermediate-CL zircon with low contrast zoning. To characterize the nature of the interface domain and to identify mechanisms of trace element mobility in metamorphosed zircon, we analyzed several specimens prepared from zircon from the Rhodope Metamorphic Complex (eastern Greece) and the Goshen Dome (western Massachusetts, USA) via atom probe tomography (APT). The data reveal three types of geochemical anomalies, each with a unique morphology. (1) Toroidal clusters with high concentrations of Pb (+ Y, Al) are found exclusively within the core of the Rhodope grain. These clusters are interpreted as decorated dislocation loops that formed during metamorphism and annealing of radiation damage to the lattice. Geochronological and geochemical data support this interpretation. (2) Complex, cross-cutting planar and linear features with anomalous concentrations of Y + P + Yb or U are spatially restricted to the core-rim interface domain; these features do not correlate with inherited geochemical variation (oscillatory zoning) or deformation-induced microstructures. Instead, the planar features likely formed in response to an interface-coupled dissolution-reprecipitation reaction that propagated into the crystal during metamorphism. The observed cross-cutting relationships are the product of either multiple events or complexity of the process that originally formed the domains. (3) Ellipsoidal features with high concentrations of Y + P + Yb (+ Al) are found exclusively within the high-Y + P + Yb planar features. These features are interpreted as the product of spinodal decomposition that occurred during exhumation as the zircon passed the solvus where local equilibria favored nm-scale exsolution to minimize the Gibbs free energy. The presence of multiple types of geochemical features in these examples indicates that trace element mobility in zircon is driven by multiple processes over the course of orogenesis. Given that these atypical domains are apparently restricted to zircon metamorphosed at *UHT* and *(U)HP* conditions, their presence may represent a marker of metamorphism at very-high-grade conditions.

Introduction

Zircon ($ZrSiO_4$) is a robust geochronometer widely used across the geosciences to determine provenance (Gray and Zeitler, 1997; Gehrels et al., 2011) and quantify the nature, timing, and rates of tectonic, magmatic, impact, and metamorphic processes (Schoene et al., 2015; Coleman et al., 2004; Reddy et al., 2015; Harley et al., 2007; Rubatto, 2017). The nature and conditions of geologic events can also be derived from a single grain through the characterization of micrometer-scale variations in crystallographic orientation, rare earth element (REE) geochemistry, or stable isotopes (e.g., Reddy et al., 2006; Rubatto, 2002; Hoskin and Schaltegger, 2003; Valley, 2003). Coupled geochronological and geochemical analyses can thus provide insights into the origins and conditions of zircon growth and recrystallization (e.g., Rubatto,

2002; Hermann and Rubatto, 2003; Kelly and Harley, 2005; Kohn et al., 2015; Kohn and Kelly, 2018).

Metamorphic rims on zircon can form as new growth onto a pre-existing grain, as an alteration of a pre-existing zircon, or via recrystallization, which either replaces or recrystallizes previously crystallized zircon (see discussion in Rubatto, 2017). New growth is typically limited by the availability of Zr in the system (Degeling et al., 2001; Kohn et al., 2015), and sources of Zr to form new zircon are generally associated with the breakdown of Zr-bearing phases (e.g., xenotime, garnet, or zircon via Ostwald ripening processes; e.g., Kohn and Kelly, 2018) or (partial) dissolution of zircon in a melt or fluid (Nemchin et al., 2001; Harley et al., 2007; Kohn et al., 2015; Kohn and Kelly, 2018). Different mechanisms of recrystallization yield distinctive features in zircon, which provides a framework for interpreting the processes responsible for producing the rims. In the diffusion-reaction process proposed by Geisler et al. (2007), a radiation-damaged zircon (> 30% amorphous) reacts with an aqueous fluid; nanoscale pores develop, and the reaction front produces inward-penetrating irregularly shaped domains and, occasionally, nanocrystalline ZrO_2. The isotopic composition of the parent zircon is often retained, and the reacted domain contains high concentrations of non-formula elements, such as Ca, Al, Fe, Mn, and, in some cases, common Pb. The degree to which crystallinity is recovered in these grains is largely controlled by the temperature of the reacting fluid.

Zircon can also recrystallize via interface coupled dissolution-reprecipitation (ICDR) reaction (Geisler et al., 2003, 2007; Tomaschek et al., 2003; Rubatto et al., 2008; Vonlanthen et al., 2012). The sub-solidus ICDR reaction is recognized as an important replacement process in metamorphic minerals that is mediated by an aqueous fluid or a melt and produces inward-penetrating irregularly shaped domains (Putnis, 2009; Putnis and Austrheim, 2010; Putnis and John, 2010; Geisler et al., 2007; Harlov et al., 2011; Vonlanthen et al., 2012; Ague and Axler, 2016). In zircon, ICDR reactions produce rims that are crystalline and epitaxial with the parent zircon; the reaction can completely reset the isotopic system and chemical attributes to produce zircon with lower minor and trace element concentrations than the parent zircon (Geisler et al., 2007; Vonlanthen et al., 2012). Zircon rims formed by the ICDR process are commonly recognized by thorite, coffinite, and xenotime inclusions within the reacted domain, and by the occurrence of μm-scale porosity (Geisler et al. 2007), though it has been established that pores can reduce in size in response to annealing (Putnis, 2002; Vonlanthen et al., 2012).

The mechanisms responsible for compositional modification of zircon occur at the atomic scale, which is a much finer spatial resolution than the analytical techniques typically applied to zircon (μm-scale). Therefore, our interpretation of geochemical processes is based on information collected at an observational scale that far exceeds that at which the processes operate, which may limit our understanding of zircon growth, recrystallization, and metamorphism. Most recently, transmission electron microscopy (TEM) and/or atom probe tomography (APT) of zircon have been used to evaluate the nm-scale redistribution of trace elements associated with radiation damage, metamorphism, and deformation (Vonlanthen et al., 2012; Valley et al., 2014; Kusiak et al., 2015; Seydoux-Guillaume et al., 2015; Peterman et al.,

2016a; Piazolo et al., 2016; Reddy et al 2016; Kusiak et al., 2018; Seydoux-Guillaume et al., 2018). These studies demonstrate that atomic scale characterization of zircon can provide new insights into the processes responsible for the chemical modification of zircon.

One aspect of zircon research that has received little attention is the set of mechanisms occurring at the interface between igneous zircon cores and the younger metamorphic rims that commonly surround them. Until recently, the small scales of these domains have precluded detailed study. In many cases, these interfaces are sharp, with discrete boundaries (e.g., Corfu et al., 2003). However, in some examples, the interface between the detrital core and metamorphic rim is marked by a thin domain that is dark in cathodoluminescence (CL) (Vavra et al., 1996; 1999; Krenn et al., 2010). In this contribution, we examine atypical interface domains in zircon that consist of a paired set of domains: a CL-dark region located immediately adjacent to the detrital core that is surrounded by a CL-bright region with complex textures and internal zoning patterns (**Fig. 1**). Metamorphic rims are located outside of the interface domain and exhibit low CL intensities and weak compositional zoning.

Complex interface domains similar to the examples in **Fig. 1** are evident in published images of zircon from multiple localities and rock types, including: felsic and intermediate intrusive rocks and pelitic and restitic schists from the Alpine Betic-Rif (Zeck and Williams, 2002); felsic garnet-kyanite granulites from the Letseng-la-Terae kimberlite (Schmitz and Bowring, 2004); *UHP* metapelitic gneisses from the Rhodope Metamorphic Complex, Greece (Liati et al., 2011; Krenn et al., 2010); metapelitic granulites from the Northern Lesotho kimberlites (Schmitz and Bowring, 2004); ultrahigh-temperature (*UHT*) metapelites from northern India (c.f., Fig. 3e,f, Taylor et al., 2015) and Rogaland, Norway (Laurent et al., 2018); and high-pressure (*HP*) granitoids in Syros (Tomaschek, 2010). The observation of similar core-rim interface domains in zircon from different orogenic systems suggests that these atypical interface domains may reflect common drivers for trace element mobility during metamorphism, and thus may have implications for the record of metamorphism extracted from zircon. Here we focus on two representative zircon grains that contain this characteristic interface domain: one is from the matrix of a garnet-kyanite metapelite from the Rhodope Metamorphic Complex near Xanthi, Greece; the other is an inclusion in a garnet porphyroblast from a restitic garnet-kyanite-phlogopite metapelite from the Goshen Dome in western Massachusetts, USA. We used APT to characterize the nanoscale structure and chemistry of these complex core-rim interface domains and evaluated the mechanisms associated with their development. We show that nanoscale features within these atypical interface domains form in response to a range of mechanisms during metamorphism at very-high-grade conditions and demonstrate how these nanoscale features can be useful in reconstructing the metamorphic history of the host rock.

Geologic background and prior sample characterization

Rhodope Metamorphic Complex, Eastern Greece

Following the classification of Janák et al. (2011), the Rhodope Metamorphic Complex (eastern Greece and southern Bulgaria) is subdivided into the Lower, Middle, Upper, and Uppermost Allochthons. The metapelite from this study is located at the base of the Middle Allochthon,

which was thrust southwest over the Lower Allochthon during Alpine convergence (Krenn et al., 2010; Janák et al., 2011); sample coordinates and locations are provided in the Supplementary Materials (Fig. S1). Metamorphic diamonds in metapelites (Perraki et al., 2006; Mposkos and Kostopoulos, 2001; Schmidt et al., 2010) indicate ultrahigh-pressure (*UHP*) metamorphism in the region (>4.5 GPa, c. 800°C; e.g., Krenn et al., 2010), but the timing and number of *UHP* events remain controversial. Some interpret *UHP* metamorphism as a single, protracted event that began c. 186 Ma (Krenn et al., 2010); others interpret several *UHP* and *HP* events from Jurassic to Eocene time (Liati, 2005; Janák et al., 2011; Kirchenbaur et al., 2011; Schmidt et al., 2010; Liati et al., 2016). $^{206}Pb/^{238}U$ dates from zircon rims in garnet-kyanite metapelites from the same locality (Krenn et al., 2010), and from a similar lithology c. 200 m away (Liati, 2005; Liati et al., 2011), have been interpreted to record metamorphism at c. 150–144 Ma. Some studies also suggest an earlier event at 158 Ma (Liati et al., 2016) and an event as late as 83 Ma (Liati, 2005).

The zircon (grain 26) examined in this study (**Fig. 2**) was previously analyzed via laser ablation split stream inductively coupled plasma mass spectrometry (LASS-ICP-MS) by Peterman et al. (2016a), with two spots located in the core and two spots in the rim. The core contains 1050 ppm U, 120 ppm Th, with a positive Ce anomaly, a negative Eu anomaly, and a steep chondrite-normalized heavy rare earth element (HREE) profile, consistent with magmatic growth (e.g., Hoskin and Ireland, 2000; Hoskin and Schaltegger, 2003). The rim has a relatively flat chondrite-normalized HREE profile, a positive Ce anomaly, and a weakly negative Eu anomaly. Measured U and Th concentrations in the rim are 450 ppm and 3 ppm, respectively. The spots measured from the core yielded highly discordant dates; the spots from the rim yielded concordant ^{207}Pb-corrected $^{206}Pb/^{238}U$ dates of 149 ± 2 and 152 ± 2 Ma (2σ), though we note that discordance can be difficult to detect in zircon younger than late Paleozoic (Spencer et al., 2016). A discordia line drawn through the concordant rim and the discordant core analyses indicates an upper intercept of 2144 ± 33 Ma, which has been interpreted as the timing of original zircon crystallization (Peterman et al., 2016a). The deposition age of the protolith at Xanthi, as bracketed by detrital zircon ages, is uppermost Proterozoic (c. 560 Ma) to pre-Hercynian (Liati, 2005; Liati et al. 2011). Apart from physical transport and deposition, no evidence of chemical alteration or other metamorphic events have been documented between original crystallization and *UHP* metamorphism; however, a second generation of zircon rims evident in some grains (see examples in **Fig. 1**) suggests additional metamorphic events following the c. 150 Ma *UHP* event (Liati, 2005; Liati et al., 2011).

Goshen Dome, Western Massachusetts, USA

Two main phases of orogenesis dominate the tectonometamorphic history of the Goshen Dome region within the northern Appalachians in western Massachusetts. The first phase involved the accretion of the Shelburne Falls and Bronson Hills Arcs against the Laurentian margin at 480–470 Ma and 460–445 Ma, respectively (Karabinos et al., 1998; Macdonald et al., 2014). During the second phase, Devonian metasediments were thrust westward over the previously accreted arc rocks, which produced regional high-temperature metamorphism associated with the Acadian orogeny (Armstrong et al., 1992). Monazite data from regional schists demonstrate a protracted

sequence of tectonic events spanning 390–350 Ma, with peak pressure attained at c. 370 Ma (Pyle and Spear, 2003; Pyle et al., 2005; Cheney et al., 2006). Garnet geochronology from the Townshend Dam in southern Vermont indicates prograde garnet growth from c. 383 Ma to 375 Ma (Gatewood et al., 2015).

The Goshen Dome, located in western Massachusetts, has been mapped as a tectonic window through an Acadian thrust sheet into gneisses and associated rocks (Hatch and Warren, 1981). The metapelite sampled in this study occurs as isolated meter to decimeter scale bodies of coarse-grained garnet-kyanite-cordierite-phlogopite schist within the Cobble Mountain Formation, which mantles the dome (location information provided in Fig. S2). Phosphatic garnet megacrysts (>3 cm diameter) found within this matrix contain abundant precipitates of apatite, ilmenite, and rutile, and have been interpreted as *UHP* relics (Snoeyenbos et al., 2011) within a matrix that was largely re-equilibrated at upper amphibolite facies. Alteration and replacement of garnet was localized along penetrative fractures and within high-Ca cores; the domain containing zircon analyzed in this study was not affected by these reactions. Zircon inclusions in phosphatic garnet display a distinctive high-Th domain immediately against the igneous cores.

The zircon grain analyzed by APT from this locality (**Fig. 3**) yielded concordant ^{207}Pb-corrected ^{206}Pb/^{238}U dates of 422–443 Ma (± 2%, 2σ; Peterman et al., 2016b); trace element concentrations measured from the same analytical volume show a positive Ce anomaly, a negative Eu anomaly, and a HREE pattern consistent with typical magmatic zoning (e.g., Hoskin and Ireland, 2000; Hoskin and Schaltegger, 2003). Uranium and Th concentrations within the core are c. 850 ppm and 400 ppm, respectively, which yielded a mean Th/U = 0.47. The rim is significantly lower in U and Th than the core, with concentrations of c. 250 ppm U and 10 ppm Th, respectively. Th/U in the rim ranges from 0.02 to 0.06. The rim is too thin to date via LA-ICP-MS, but other zircon rims in the same petrographic context yield concordant dates consistent with two stages of growth at 400 to 396 Ma (potentially *UHP*; see discussion in Peterman et al., 2016b) and 385 to 373 Ma.

Methods

Sample characterization by electron microbeam

Both zircon grains were initially characterized using CL and backscattered electron (BSE) imaging. Thin sections were coated with a thin (<10 nm) layer of carbon to minimize charging and CL images were collected at Bowdoin College on a Tescan VEGA3 SEM with a Rainbow CL detector. CL images were collected in either panchromatic or ColorCL mode; both modes used the same operating conditions: 15–16 mm working distance, with a 10 kV, c. 250 pA beam. Each grain was also characterized by electron backscatter diffraction (EBSD) to evaluate variations in crystallographic orientation across the grains. Prior to EBSD analysis, thin sections were weighted with a halved brass rod and polished for 3 hours in a non-crystallizing colloidal silica suspension on a Buehler Vibromet2 vibratory polisher (SYTON method of Fynn and Powell, 1979). Thin sections were re-coated with 5 nm carbon to minimize charging; EBSD data were collected using NordlysMax^2 detectors on the SEM at Bowdoin College and on a Tescan MIRA3

field emission SEM at Curtin University. Both SEMs were operated under high vacuum at 20 kV. At Bowdoin, a 15 nA beam current and 50 ms/frame were used for EBSD collection, whereas a 1nA beam current and 25 ms/frame were used at Curtin. All EBSD data were acquired using AZtec and post-processed with Channel 5.12 software.

Compositional maps were collected using the UMass-Amherst CAMECA UltraChron electron microprobe (EPMA) operated at 15 kV, 300 nA. Although the Rhodope grain analyzed by APT in this study was not characterized by EPMA, compositional data from representative grains from this locality are included in the Supplementary Materials (Fig. S3).

Sample preparation for atom probe tomography

Atom probe specimens of the Rhodope zircon grain were prepared from two transects across the core-rim interface. The first transect includes APT specimens 57082_z26 M1–M8 (blue-rimmed dots, **Fig. 2**) some of which were described in Peterman et al. (2016a). The second traverse includes APT specimens 57082_z26 M12–M17 (red-rimmed dots, **Fig. 2)** and extends from the CL dark-domain (M12–M14) into the core (M15–M17). Specimens were also prepared from a portion of the CL-dark domain within the Goshen Dome zircon (pink dots; M14 and M15, **Fig. 3**).

Regions of interest for APT within zircon were identified by producing a 9 x 9 μm compositional map via time-of-flight secondary ion mass spectrometry (ToF-SIMS) using a Tofwerks C-ToF detector on the Tescan LYRA3 focused ion beam (FIB)-SEM at Curtin University operated at 500 pA, with a 20 kV Ga^+ ion beam. Positive ions were collected and SIMS maps were produced using Tofwerks Explorer version 1.30 for ^{89}Y ions. Cross-correlation of the ToF-SIMS map with EPMA, CL, and secondary electron images ensured that the targeted sample locations within the region of interest were extracted for APT analysis. To mark the target locations for preparing specimens for APT, we deposited Pt buttons approximately 50 nm in diameter on the zircon surface along the interface domain.

Needle-shaped APT specimens were prepared using a Tescan LYRA3 FIB-SEM. The procedure for site-selective sample lift-out and tip-sharpening was adapted from methods described by Thompson et al. (2007). Final atom probe specimen tip diameters were <150 nm, and the half-shank angles were 6° to 10° (full details included in **Table 1**). All specimens were oriented normal to the polished crystal face (**Fig. 1**). Ga implantation associated with the initial stages of FIB milling at 30 kV was minimized by a final polishing annulus with a beam energy of 5 kV.

Atom probe tomography analysis

APT was undertaken at the Geoscience Atom Probe laboratory, housed in the John de Laeter Centre, Curtin University. Specimens were analyzed using a CAMECA local electrode atom probe (LEAP) 4000X HR equipped with a pulsed laser and a reflectron to enhance isotopic resolution. Optimization of APT analysis of zircon on this instrument is described by Saxey et al. (2018). Full operating conditions are listed in **Table 1** and summarized here. Each specimen was cooled to ~60 K under ultrahigh vacuum (10^{-11} torr), with a high voltage applied to facilitate

field evaporation of atoms from the tip surface. A fine, ultraviolet (λ = 355 nm) laser was focused on the specimen apex and pulsed at 200 kHz, with an energy of 100 pJ per pulse, to control the ion evaporation process. The voltage was gradually increased during the analysis from c. 3 to 10 kV to maintain an average ion detection rate of 0.006 to 0.008 ions per pulse. Ions were recorded on a position-sensitive detector, and the composition was determined using time-of-flight mass spectrometry. This information, coupled with the order of detector events, was used to reconstruct the 3-D position and composition of atoms within the specimen with sub-nanometer spatial resolution. Each specimen yielded approximately 4×10^7 ions. The primary zircon components (Zr, Si, O, and Hf) commonly field evaporate as molecular oxides, whereas Pb evaporates in its elemental form (**Fig. 4;** raw spectra for all specimens are provided in Supplementary Figure S7). The mass resolving power for each dataset was c. 1000 (full width at half maximum for $^{16}O_2^+$). Data reconstruction and analysis were performed using IVAS (Integrated Visualization & Analysis Software; version 3.6.12) from CAMECA Instruments. Spatial reconstruction parameters (**Table 1**) were based on empirically derived values from prior experiments on reference zircon (Saxey et al., 2018). All zircon analyses were ranged for Pb, Y, and U (**Fig. 4**; see also Supplementary Figure S7). Yb is used as a proxy for the HREE in the APT reconstructions; other HREE are difficult to measure because of either overlapping peaks or dilution of the REE peaks across multiple elemental and molecular species. Compositional analysis was performed using IVAS; 1σ uncertainties were determined using the counting statistics of each ranged peak and their background correction. The compositions of sub-domains (**Tables 2, 3**) were extracted using isoconcentration surfaces or cylindrical domains (Hellman et al., 2000).

Transmission electron microscopy

A Tescan Lyra 3 FIB–SEM was used to produce a site-specific lift out of a lamella for transmission electron microscopy (TEM) studies. An approximately 10-µm wide region containing the core-rim interface domain was lifted out and mounted onto a copper grid. The lamella was then thinned to approximately 100 nm, followed by a low voltage (2 kV) "clean up" routine to remove surface damage. The electron transparent lamella was used for TEM analysis on an FEI Talos FS200X G2 TEM/scanning TEM (STEM) microscope operated at 200 kV and equipped with a Super-X energy dispersive spectroscopy (EDS) system. Bright field (BF) and high-angle annular dark-field (HAADF) imaging in STEM mode were used to image the sample. EDS maps were collected for 10 minutes with a beam current approximately 0.6 nA.

Results

The characteristics of the atypical interface domain are nearly identical in both grains, from the micrometer to nanometer scale. Here we highlight the key attributes of both zircon grains measured by SEM and EPMA. Next, we compare the compositions of the specimens as measured by atom probe. Lastly, we describe the four types of nanoscale features observed (**Table 2**) and their distributions across spatial domains within the zircon (core, rim, or interface). Regarding terminology, we use "domain" to refer to µm-scale regions that are distinguished by chemistry or CL intensity; "feature" refers to nanoscale anomalies within the APT specimens. Trace element concentrations of each specimen and of select nanoscale features

are reported in **Table 3** with 1σ uncertainties. Animated reconstructions of each specimen are included in the Supplementary Materials.

SEM + EPMA

Rhodope zircon

The core of zircon grain 26 exhibits oscillatory zoning visible in CL and BSE images (**Fig. 2**), which is interpreted to reflect trace element variation during growth (e.g., Vavra et al., 1999; Corfu et al., 2003). This grain exhibits CL variation within the rim domain, but it is lower contrast than the core. The interface domain between the core and rim measures up to 5 μm; it is thickest at the tips of the zircon and absent from the mid-section of the grain. EBSD analysis indicates that the grain is crystalline with the same band contrast (pattern quality) values from all domains, with no intragrain misorientations within the 0.5° analytical uncertainty (Peterman et al., 2016a). EBSD analyses of additional zircon grains from this sample yield the same uniformity of crystallographic orientation across all domains (Supplementary Materials, Fig. S4). EPMA compositional maps show that the CL-dark portion of the interface domain has high concentrations of Y, P, and U, whereas the CL-bright portion has lower U concentrations (Peterman and Snoeyenbos, 2015; see Supplementary Materials, Fig. S3).

Goshen Dome zircon

The core of the Goshen Dome zircon grain shows complex oscillatory zoning with internal truncations (white dotted lines in **Fig. 3**). Fractures displace fragments of the zircon by c. 5–10 μm (blue dotted lines, **Fig. 3**) and are filled by CL-dark zircon (high U, low Y). The interface domain surrounds the core and the displaced fragments, indicating that it postdates fracture development. In contrast with the CL-dark filled fractures, the CL-dark portion of the interface domain is high U + Y + Th. The CL-bright portion exhibits complex, convolute CL variations and is low U. The high-U rim yields low contrast, intermediate CL intensities with patchy zoning. EBSD analyses show that although the grain was broken in to several fragments that are at different orientations, crystallographic orientations are uniform across all domains within a given fragment.

Atom Probe Tomography

Specimen compositions

The primary components of zircon (Zr, Si, O, and Hf) are homogeneously distributed in all atom probe specimens (**Table 3**). Trace element concentrations are significantly higher in the CL-dark portion of the interface domain than any other domain. For the Rhodope grain, U concentrations are typically twice as high in the core as in the rim and are even higher in the CL-dark domain. Yttrium concentrations are an order of magnitude higher in the CL-dark domain than the core or rim. Phosphorous concentrations are lowest in the rim, moderate in the core, and higher than 500 ppma in some tips from the CL-dark domain. At the scale of the entire specimen, Al is below detection in all specimens except Rhodope M14; Ti varies between 58 and 71 ± 1 ppma among all specimens.

Homogeneous specimens

Two specimens contain no nanoscale features. Extracted from the rim, Rhodope M8 measures c. 250 nm long (Fig. 5a) and U is homogeneously distributed at 34 ± 1 ppma. Rhodope M7 was prepared from the CL-bright portion of the interface domain and also measures c. 250 nm (Fig. 5b); U is homogeneously distributed, but at marginally higher concentrations (49 ± 1 ppma). The measured U concentrations are lower than those reported by LASS, so it is possible that U concentrations are heterogeneous at a scale larger than the APT specimen, but smaller than the LASS spot. The rim composition is variable, as documented by variation in CL emission, and the concentrations reported by LASS reflect the average composition across these variable domains. Therefore, the lower U concentrations measured by APT may simply reflect a low-U location within the rim, particularly when considering that the volume of the LASS spot is > 6 orders of magnitude greater than the volume of an APT specimen.

Toroidal clusters

Ten < 25 nm diameter clusters (some < 10 nm) with a toroidal geometry and high concentrations of Pb + Y (+ Al) were observed within specimens prepared from the zircon core (Rhodope M15, M16, and M17). M16 contains six of these clusters (Fig. 5c); M15 and M17 each contain two (Fig. 5d, e). The clusters are heterogeneously distributed within each specimen and are absent from all atom probe specimens outside the core. No other elements are found within these geochemically anomalous features (**Table 3**) and all other trace elements measured above background are homogeneously distributed in the volumes outside the clusters, including U (c. 71 ± 1 ppma). These observations are identical to those described in other APT specimens prepared from the core (Peterman et al., 2016a).

High-Y and low-Y planar features

Planar features defined by anomalous concentrations of Y, P, Yb, and U are found exclusively within the CL-dark portion of the interface domains (Figs. 6-9). The trends in Yb and P mimic those observed in Y, but the features are best observed within Y reconstructions because of more favorable signal-to-noise. Within a specimen, many planar features are parallel to one another, but some low-Y planar features intersect or cross-cut other Y features. For example, Rhodope M6 contains four high-Y planar features (I–IV) and four low-Y planar features (1–4) (Fig. 6). High-Y features I and II are parallel to each other and spaced c. 50 nm apart (see Supplementary Materials for 3-D rendering); features III and IV are oriented differently from features I and II, but none of these high-Y features intersect or cross-cut. In contrast, the low-Y planar feature 2 cross-cuts features 1 and IV, which are low Y and high Y, respectively, and low-Y features 3 and 4 cross-cut high-Y features I and II. In contrast, Rhodope specimen M12 (Fig. 7) contains three planar features that are relatively low in Y + P + Yb, none of which intersect. Some planar features, such as those in Rhodope M13 and M14 (Figs. 8-9), have complex intersecting relationships.

Specimens prepared from the CL-dark portion of the interface domain of the Goshen Dome grain also contain planar features that are high Y + P. Most of Goshen Dome M14 is high Y + P and contains several parallel high-Y + P planar features (Fig. 10a; **Table 3**). There is an irregular contact between the high-Y planar features and the low-Y feature at the bottom of the specimen;

this irregular boundary truncates the high-Y + P planar features. Goshen Dome M15 (**Fig. 10b-d**) contains three parallel, planar features with relatively diffuse boundaries. The most prominent feature is near the bottom of the specimen and is a 50 nm thick planar feature that is low in Y and P (**Table 3**). In contrast with the other specimens, the relative difference in concentrations between the high- and low-Y features is only c. 2% (**Table 3**).

High-U planar features

Some specimens from the CL-dark portion of the interface domain contain high-U planar features that are 5-16 times as enriched in U as the remainder of the specimen. In Rhodope M12 (**Fig. 7**), the high-U planar features are located near the low Y + P + Yb planar features, but not coincident; they contain similar Y + P + Yb concentrations as the whole specimen (**Table 3**). In Rhodope specimen M13 (**Fig. 8**), the two high-U planar features are oriented at an angle to each other, but do not intersect. The thin, planar to curviplanar, high-U features in Rhodope M14 (**Fig. 9**) contain > 6 times the U concentration measured for the specimen and are also high-Pb (**Table 3**). Most of the high-U features do not extend across the entire specimen; they are arranged at a variety of angles with respect to the z-axis of the specimen and some intersect.

Ellipsoidal Features within Planar Features

Three of the atom probe specimens prepared from the CL-dark portion of the interface domain exhibit ellipsoidal clusters with high trace element concentrations (**Figs. 7-9**). In contrast with the Pb clusters in the core, these ellipsoidal features are not toroidal and contain significantly lower concentrations of Pb (**Table 2**). The ellipsoidal features are exclusive to and heterogeneously distributed throughout the high-Y + P + Yb planar features and are conspicuously absent from the low-Y + P + Yb + Al planar to curviplanar features. Details within the ellipsoidal features are best expressed in the Y dataset because of signal-to-noise, but reconstructions of Yb and P yield similar spatial distributions. In Rhodope M12 and M13 (**Figs. 7, 8**), the ellipsoidal features contain nearly an order of magnitude higher Y and P concentrations than the local background, and a factor of six to eight higher Yb (**Tables 2, 3**). Lead is also found within these features, despite being below background in the mass/charge spectra for the whole specimen (**Table 3**). Some of the ellipsoidal features are lenticular, which can be an artifact of reconstruction due to different evaporation fields between the cluster and the zircon matrix (see discussions in Devaraj et al., 2014 and Fougerouse et al., 2016). However, the orientation of the flattened geometry of these features is not in a direction consistent with that predicted for artifacts associated with differential field evaporation. The ellipsoidal features are not found in any of the low-Y or low-U planar features. As with Rhodope M12, most of Rhodope M14 (**Fig. 9**) is high in Y + P + Yb; this specimen is also high in Al. Ellipsoidal features with very high-Y + P + Yb + Al concentrations are abundant and heterogeneously distributed throughout the specimen and are conspicuously absent from the low-Y + P + Yb + Al planar to curviplanar features. In most cases, Al follows Y (black arrows, **Fig. 9**), but there are some locations where Al is not coincident with high-Y + P + Yb (blue arrows, **Fig. 9**).

Linear features

Approximately 5 nm above the high-U curviplanar feature in Rhodope M6 (**Fig. 6**) is a 30 nm long linear feature with > 30 times the U concentration as the whole specimen. The linear feature does not intersect the curviplanar feature and, whereas the high-U feature is low in Y + P, the linear feature contains > 50% more Y and 1600 ppma Al (**Table 3**). For comparison, Al is below detection in the rest of the specimen. Goshen Dome M14 (**Fig. 10a**) also contains a linear feature decorated in Y; it lacks U enrichment and is located within the low-Y portion of the specimen.

Transmission Electron Microscopy

The thin foil extracted across the core-rim boundary of the Rhodope zircon (see annotation in **Fig. 2a**) by FIB-SEM and analyzed by TEM reveals heterogeneously distributed toroidal structures that measure 10 to 150 nm in diameter (see arrows in **Fig. 11a, b**). The toroidal features are only evident in the core; they are absent in the interface and rim domains. A Z-contrast image collected using a HAADF detector (**Fig. 11c**) shows several bright spots c. 5 to 10 nm in diameter. Compositional analysis of the same region by EDS shows that these bright spots are high in Pb (**Fig. 11d**) with homogeneous Zr, Si, O, Hf, and Y (see Supplementary Materials. Fig. S5). Pb concentrations are near the lower limit of detection for EDS and thus are only above background noise in the highly concentrated regions. As observed in a dark field image of the entire TEM foil, the core-rim interface domain contains numerous dislocations (see Supplementary Materials, Fig. S6).

Discussion

The features observed in the zircon grains can be classified by their spatial context. First, Pb clusters are found exclusively within the core, which has implications for Pb mobility during metamorphism. Second, the nanoscale planar, ellipsoidal, and linear features are all restricted to the interface domain, which leads to an evaluation of the processes likely responsible for trace element mobility in these grains. Third, the attributes of the rim domain are linked to the likely process(es) by which they formed in these grains.

Toroidal Pb clusters

Every specimen prepared from the core of the Rhodope zircon grain (both this study and Peterman et al., 2016a) contains heterogeneously distributed toroidal clusters with elevated Pb, Y and Al, which requires a mechanism that accounts for both Pb mobility and entrapment. Nanoscale Pb enrichment in zircon has been previously documented by Kusiak et al. (2013; 2015) and Valley et al. (2015) and differences in the spatial distribution and trace element characteristics of these Pb clusters suggest multiple mechanisms for Pb clustering. Kusiak et al. (2015) documented heterogeneously distributed Pb clusters and diffraction analysis led to the interpretation that these features are metallic Pb that formed in response to thermal annealing, crystal recovery, and phase separation of coexisting silicate and lead melt. Despite similarities in the spatial distribution, the Pb clusters identified in this study and Peterman et al. (2016a) are zircon enriched with Pb, not pure Pb metal. The phase separation model also does not account for the toroidal morphology that we observed. Valley et al. (2015) found 10 nm diameter

clusters of Pb + Y + REEs, spaced 10 to 40 nm apart in Archean and Hadean zircon; these clusters were interpreted to have formed by diffusion of these elements into amorphous domains produced by damage from alpha-recoil. We similarly suggest migration of Pb, but we argue that the toroidal morphology and heterogeneous distribution of Pb clusters is best explained by Pb entrapment in dislocation loops.

Dislocation loops can form through the well-studied phenomenon of annealing of α-decay induced radiation damage in zircon (e.g., Bursill and McLaren, 1966; Murakami et al., 1991; Nasdala et al., 1998, 2001, 2002; Meldrum et al., 1998; Zhang et al., 2000a, b; Geisler, 2002; Ewing et al., 2003; Geisler et al., 2007). Some of the earliest experiments showed that increased *T* can significantly recover accumulated radiation damage to the zircon lattice and promote the development and migration of dislocation loops through the zircon structure (Bursill and McLaren, 1966). The extent of recovery depends upon both the structural state of zircon at the time of annealing and on the conditions of annealing (e.g., Nasdala et al., 2002). As summarized by Ewing et al. (2003), highly damaged, but non-metamict zircon is understood to undergo a two-stage structural recovery process involving recovery of short-range defects followed by epitaxial recrystallization at higher temperature (> 727°C; Zhang et al., 2000a, 893°C, Geisler et al., 2001). In metamict zircon, thermally induced annealing occurs in three stages (Geisler, 2002). As with non-metamict zircon, the first stage involves anisotropic recovery of short-range order and point defects; amorphous domains remain within highly crystalline zircon at this stage. The second stage is accomplished by epitaxial recrystallization along the internal amorphous-crystalline boundaries. During the third and final stage of structural recovery, stable point defects are removed, and the remaining amorphous domains recrystallize to produce a fully crystalline zircon. In addition to high temperature annealing, experiments with natural zircon revealed that zircon undergoes partial structural recovery during storage at geologic conditions, even at temperatures below 300°C (Meldrum et al., 1998; Geisler et al., 2001; Nasdala et al., 2001; 2004); the presence of fluids strongly enhances the kinetics of recovery (Geisler et al., 2003; 2007). The annealing of fission tracks in zircon also indicates some lattice recovery under relatively low-temperature geologic conditions (Garver et al., 1999).

As increased *T* enhances Pb mobility within zircon (Cherniak et al., 1991), particularly in radiation damaged zircon, thermally induced annealing during prograde metamorphism provides an excellent explanation for the entrapment of mobile Pb within migrating dislocation loops. Once Pb is trapped, it preserves the loop, thereby explaining the toroidal morphology of the clusters. This interpretation is bolstered by the observation of 10 to 150 nm diameter dislocation loops via TEM and clusters of Pb enrichment detectable by EDS (>0.1 wt %) at the same scale as many of our clusters (c. 10 nm). The lack of large (up to 100 nm) dislocation loops within the APT specimens is likely a function of the analytical volume of each atom probe specimen and the heterogeneous distribution of dislocation loops within the zircon.

Enhanced Pb mobility due to increased *T* during prograde metamorphism can also lead to Pb loss. Therefore, we interpret that prograde metamorphism best explains the geochronologic data measured by LASS and APT (Peterman et al., 2016a), the loss of >75% radiogenic Pb, the

production of dislocations loops during annealing, and the production of discrete Pb reservoirs in crystalline, yet discordant, zircon. Furthermore, the $^{207}Pb/^{206}Pb$ ratios measured from the clusters are consistent with metamorphism at c. 150 Ma (Peterman et al., 2016a), which argues against exsolution shortly after crystallization (e.g., nano-exsolution, as observed in monazite; Fougerouse et al., 2018; Seydoux-Guillaume et al., 2019). Although the data derive from a single zircon, the features are reproducible, and the proposed mechanisms may also occur in other radiation-damaged, discordant zircon grains.

It remains unknown if Pb-rich toroidal clusters exist in the Goshen Dome grain because the core was not sampled. However, if structural recovery of zircon via recrystallization is a prerequisite for forming such clusters, there was likely insufficient radiation damage accumulated by the time of metamorphism to drive Pb-toroid formation in the Goshen Dome zircon because of both the relatively short interval between original crystallization and metamorphism (c. 50 Ma) and the low U + Th concentrations. Calculations of the effective α/g at the time of metamorphism for the Rhodope grain indicate 8.0 x 10^{18} α/g as compared with 1.0 x 10^{17} α/g for the Goshen Dome grain (**Table 4**). For reference, the first percolation point, wherein amorphous domains form an interconnected network within radiation damaged zircon, occurs with a dose of ~2.2 x 10^{18} α/g (Pidgeon, 2014; revised down from 3.5 x 10^{18} α/g, proposed by Salje et al., 1999). At dosages of 5 x 10^{18} α/g (Pidgeon, 2014), which corresponds to Stage 2 of Murakami et al. (1991), zircon is considered fully metamict and amorphous material is the main component of zircon. The mechanisms for the formation of dislocation loops and enhanced Pb mobility are consistent with the high radiation dose calculated for the Rhodope grain at the time of metamorphism and provide sufficient driving force for the reaction. These data also suggest that clusters should not be expected in grains with lower radiation doses at the time of metamorphism, such as the Goshen Dome grain.

Table 4: Radiation damage calculations

	Crystallization (Ma)	Metamorphism (Ma)	U (ppm)	Th (ppm)	Total α/g	α/g post-metm.[1] event	Effective α/g at time of metm.
Rhodope							
core	2144 ± 33 Ma	150 Ma	1050	120	8.6 x 10^{18}	6.2 x 10^{17}	8.0 x 10^{18}
rim	150 Ma	-	450	3	2.0 x 10^{17}	na	na
Goshen							
core	440 ± 9 Ma[2]	400 to 385 Ma	850	400	1.5 x 10^{18}	1.4 x 10^{18}	1.0 x 10^{17}
rim	400 to 385 Ma	-	250	10	2.5 x 10^{17}	na	na

[1]metm. = metamorphism

[2]maximum crystallization age used in calculations

Processes driving trace element mobility within the atypical interface domain

Whereas the atom probe specimen from the CL-bright portion of an interface domain is homogeneous and lower in trace element concentrations, *all* specimens from the CL-dark portion of the interface domain contain geochemically anomalous features that indicate trace element mobility. Each feature morphology has a characteristic geochemical profile (**Table 2**), which suggests a sequence of nanoscale processes. Here we evaluate which processes best explain the anomalous nanoscale features observed among specimens from these grains.

Planar features

All atom probe specimens from the CL-dark band within the interface region contain planar features with high (and low) concentrations of U and Y + P + Yb (+ Al), some of which are parallel whilst others intersect one another (e.g., **Fig. 6b**). Because planar features are not uncommon in zircon, we evaluate the possibility that these planar features are the nm-scale manifestation of μm-scale features, such as oscillatory zoning, healed fractures, dislocations, or low-angle boundaries.

Oscillatory zoning within zircon correlates with trace element variation during original crystallization (e.g., Hanchar and Miller, 1993) and the temperature of crystallization (Melnik and Bindeman, 2018). The trivalent REEs, in particular, Dy^{3+}, are the dominant CL activator in zircon, whereas the presence of U^{4+} and the radiation damage induced from its decay suppress CL emission (e.g., Nasdala et al., 2003 and references therein). In these samples, the core exhibits high-contrast oscillatory zoning; the rim has some variation in CL, but it is much lower contrast than the core. Although the interface domain contains both CL bright and dark domains, the zoning is irregular, not planar. Therefore, if oscillatory growth zoning were the source of the nm-scale planar features measured by APT, these features should be best expressed in specimens prepared from the core. Instead, planar features are absent from all specimens prepared from the core and the rim; they are exclusive to the atypical interface domain. It is conceivable that nm-scale oscillatory zoning occurs within the zircon core and that we simply did not measure this variation because the REE are difficult to accurately deconvolve in APT data, owing to peak overlap and splitting of the compositional signal across multiple molecular species (Saxey et al., 2018). However, variations in U also affect CL emission and are known to correlate with oscillatory zoning. Therefore, the presence of both high- and low-U features within the interface domain and the lack of any planar features from the core indicate that either variation in the concentrations of trace elements that affect CL emission is not resolvable via APT or that the scale of the oscillatory zoning is too large to be captured within an atom probe specimen. Additionally, the μm-scale oscillatory zones observed in CL and BSE (**Figs. 1, 2, 3**) truncate one another, but they do not intersect. In contrast, some of the planar features observed in the APT specimens intersect (e.g., **Fig. 6b, 8**), which is consistent with these features being produced by recrystallization, not original crystallization.

The CL-dark healed fractures in the Rhodope and Goshen Dome grains (light blue dotted lines in **Fig. 2b, 3**, respectively) are significantly larger than the scale of the APT reconstructions, but it is possible that the planar features in the APT data are a nm-scale manifestation of the healed fractures. In both grains, the healed fractures extend from the core towards the interface, but do not cross into the CL-bright portion of the interface domain (see BSE image in **Fig. 3**) and are not evident in the rim. The EPMA compositional maps from the Goshen Dome grain demonstrate that the healed fractures are high-U and very-low-Y, which contrasts with the composition of the planar features measured at the atomic scale, most of which are high-Y + P. Although the compositions of the healed fractures in the Rhodope grain were not measured, we infer similar variations in trace element concentrations. The compositional mismatch between

the planar features in the APT specimens and the healed fractures indicate that the features are not related. The high-U planar features may be the products of U accumulation along nano-fractures, but because some are high-Y and others are low-Y (**Table 3**), they are likely unrelated to the µm-scale healed fractures. Furthermore, although we cannot determine if the healed fractures extend into the CL-dark band, they clearly do not extend into the CL-bright domain, which suggests that they predate the formation of the interface domain.

Planar and linear accumulations of trace elements within minerals can be produced along low-angle boundaries and dislocations respectively. Examples of trace element enrichment along low-angle boundaries and/or dislocations have been reported in zircon (U, Y, Al, Be, and/or Mg; Reddy et al., 2016; Piazolo et al., 2016; La Fontaine et al., 2017), titanite (Mg, Al, K, and Fe; Kirkland et al., 2018), pyrite (Ni, Co, As, and Pb; Fougerouse et al., 2019), and baddeleyite (Fe and Si; White et al., 2017). Low-angle boundaries can develop during growth (Klapper, 2010) or as a result of deformation (Reddy et al., 2007; Timms et al., 2012), including impact-induced shock metamorphism (Reddy et al., 2016). EBSD analysis of the Rhodope grain shows no misorientation across the interface domain (Peterman et al., 2016a) and results from other grains in this sample confirm that the core, rim, and interface domains are crystallographically continuous within the 0.5° analytical uncertainty (see Supplementary Materials, Fig. S4). Results from EBSD analysis of the Goshen Dome grain are considerably more complicated as the grain is cut by numerous fractures that produce discrete variations in lattice orientation. The specimens in this study, however, are from a fracture-free, crystallographically continuous domain with no significant misorientation (**Fig. 3**). These data demonstrate that trace element accumulation along deformation-related low-angle boundaries does not explain the planar compositional features observed in these specimens. Trace element accumulation along dislocations, however, may explain the presence of linear features; this is discussed in the ***Linear features*** section.

A fluid-mediated reaction front (e.g., ICDR) may provide a mechanism for trace element accumulation along planar features. One product of the ICDR reaction of a zircon solid solution is the development of trace element enriched precipitates along the interface (Soman et al., 2010). In these experiments, the parent zircon ($zircon_{ss}$) reacts with a solution to produce a rim of zircon with a lower concentration of the solid solution phase (e.g., coffinite, thorite, xenotime) and a precipitated $zircon_{ss}$ enriched in the components of the solid solution phase (e.g., U, Th, Y) along the reaction front. If the reaction goes to completion (i.e. the eutectic is reached), near end-member zircon ($ZrSiO_4$) and the solid solution phase will coexist; the compositions of materials produced prior to reaching the eutectic depend on the composition of the parent zircon and are predicted to contain a few mol. % of the solid solution phase. The planar features observed in APT may thus represent precipitated $zircon_{ss}$ that formed as a product of the ICDR reaction; in this case, the precipitated $zircon_{ss}$ is enriched in Y and P, the primary components of xenotime (YPO_4).

As described by Geisler et al (2007), criteria for recognizing ICDR reactions include: the rim and reaction domain are epitaxial with the core; reacted domains are isotopically reset (e.g., no

inheritance); reacted domains are lower in minor and trace element concentrations; interconnected porosity is found within the interface and rim domains; and aggregates of zircon microcrystals or inclusions of thorite, coffinite, or xenotime are found within the interface domain. Our findings are consistent with many of these criteria. EBSD data show that the interface and rim are epitaxial with the core and LASS data are consistent with isotopic resetting. The rim contains significantly lower trace and minor element concentrations than the core and the CL-dark portion of the interface domain contains higher concentrations of some trace elements—notably U, Y, P, and Yb—as measured by EPMA and APT. Similar nanoscale domains that are highly enriched in trace elements and located along the ICDR reaction front have been documented in experimentally treated monazite (Harlov et al., 2011) and are predicted as an intermediate product of ICDR in altered zircon (Soman et al., 2010).

Our results diverge from the predicted characteristics of ICDR in two ways. First, the interconnected porosity required for ICDR is not evident in either zircon grain in this study, and second, the reaction domain lacks aggregates of zircon microcrystals or inclusions of thorite, coffinite, or xenotime. Evidence of nanoporosity may be destroyed by closure or eradication of pores during subsequent metamorphic events, as suggested by Ague and Axler (2016) to explain the lack of porosity in *UHP* garnet from Erzgebirge. Experimental work with monazite showed that interconnected nanoporosity can be transient or intermittent and thus not found in the final reacted products (Harlov et al., 2011). Regarding the lack of microcrystals or inclusions, if the eutectic between zircon and xenotime was not reached, inclusions are not expected to be present; instead, the products of the reaction should be near end-member zircon and trace-element enriched zircon along the interface (Geisler et al., 2007; Soman et al., 2010).

Based on these arguments, we propose that the planar features are the products of ICDR reaction fronts propagating into zircon in solid solution with xenotime. Under typical magmatic conditions, zircon can crystallize with up to 10 mol. % xenotime and remain a single phase because the relatively slow diffusion of cations in zircon at crustal temperatures (Cherniak and Watson, 2003) prevents exsolution of the xenotime component within zircon under most magmatic and moderate-grade metamorphic conditions (pink and blue curves in **Fig. 12a**, modified after Tomaschek, 2010). Pressure has the opposite effect to temperature such that the miscibility gap increases along a high dP/dT trajectory. We therefore hypothesize that the planar features were produced by local segregation of the zircon into zones of high and low concentrations of xenotime components during prograde metamorphism along a high-P, low-T path (**Fig. 13**). We interpret that the segregation was driven by a fluid-mediated ICDR process and the irregularly shaped contact between the igneous core and the CL-dark domain suggests that the reaction progressed from the rim into the zircon; the CL-dark domain marks the inward limit of the reaction front. The geochemistry and structural state of the interface domain and the rim are consistent with ICDR reaction, and the presence of the planar features exclusively along the interface boundary is also consistent with ICDR (Geisler et al., 2007; 2010; Soman et al., 2010; Harlov et al., 2011). The observation that most of the planar domains are parallel to one another is consistent with a crystallographic control on their orientation. Some sets of planar features are cross-cutting or intersect, which could indicate a sequence of ICDR reactions or could result

from accumulations of trace elements along different lattice orientations or along nanofractures. Because we cannot directly measure the lattice orientations of these features, there are insufficient data to resolve among these mechanisms for producing cross-cutting relationships.

Ellipsoidal features

Ellipsoidal features—Y + P + Yb (± Al)—are only found within regions with high concentrations of these same trace elements. Planar features with low trace-element-concentrations are notably devoid of ellipsoidal features. Although Rhodope M14 appears to be an exception to this trend, we interpret that nearly the entire specimen is a single c. 500 nm thick planar feature with high-Y + P + Yb (± Al) that also contains high-U planar features. Therefore, all ellipsoidal features are distributed heterogeneously and located exclusively within Y-rich planar features. This spatial relationship indicates a correlation between Y concentration and ellipse formation that is best explained by spinodal decomposition as the zircon crossed the chemical solvus during exhumation to the mid-lower crust. For spinodal decomposition to occur, the zircon must have been significantly enriched in xenotime components (perhaps only locally) prior to crossing the chemical solvus during exhumation (**Fig. 12**). In these grains, we suggest that an initial enrichment occurred early in the metamorphic history via ICDR reaction fronts propagating into the grain towards the core. The products of this reaction front are the trace element enriched planar features within the interface domain. As the rock exhumed to the mid-lower crust, it crossed the zircon + xenotime chemical solvus, and these features were sufficiently enriched with xenotime components that the Gibbs free energy–composition curve had a negative curvature, which catalyzed the spontaneous formation of ellipsoidal clumps within the high-Y + P planar features via spinodal decomposition (**Fig. 12b**). The presence of Al co-located within some of the ellipsoidal features suggests that some planar features were enriched in both xenotime components and the interstitial elements that aid in charge balance (Hanchar et al., 2001; Hoskin and Schaltegger, 2003) or may reflect an additional reaction.

This model successfully explains the spatial correlation between ellipsoidal domains and high concentration planar features. Importantly, it does not require an external driving force—the reaction is spontaneous because the prior ICDR reactions produced planar features enriched in xenotime components, which serve as local "parent" zircon for this reaction and drive the zircon composition into the spinodal domain. This model also explains why the low-Y planar features lack the ellipsoidal features; in contrast with the enriched planar features, the low-Y features are metastable and should not undergo spinodal decomposition. The production of the ellipsoidal features is thus part of the zircon response to decreases in P (and T) during exhumation as the sample crossed the chemical solvus. Because the ellipsoidal clumps are spatially restricted to the interface domain, they are not related to radiation damage or the repair of the crystal lattice. Rather, they represent the preservation of a series of atomic-scale reactions that record the process of zircon re-equilibration during exhumation.

Linear features

Two atom probe specimens contain linear features 50 to 100 nm long with high concentrations of either Y (M14, WMBTS-z01) or U (M6, 57082-z26). In other examples where high-Y domains

in zircon have been observed, Y is normally accompanied by Pb ± Al ± Yb ± Mg ± Be (Valley et al., 2014, 2015; Piazolo et al., 2016; Reddy et al., 2016; La Fontaine et al., 2017). Linear features with high-concentrations of U have not been reported in prior studies. The simplest explanation of how these linear features formed is accumulation along a crystal defect. Crystal defects can form in a variety of ways, including as a product of deformation, a result of radiation damage, or a defect in original growth. The linear features observed in the APT reconstructions are not ubiquitous among or within specimens from a single specimen, and yet are found in two samples with significantly different radiation doses (**Table 4**). Therefore, it is unlikely that the crystal defects were produced by radiation damage. They are also unlikely to be products of deformation as there is no measured misorientation across these grains. Instead, the linear features resemble dislocations that we interpret formed during original growth, not deformation or metamorphism. We suggest that U or Y was mobilized by the fluids associated with the ICDR reaction front and then migrated to these defects where they remain trapped, thereby preserving the defect. Fluid-mobilization of U and accumulation along nanofractures may also explain the high-U planar features in some examples, but the planar features may also result from complex segregation or ICDR reactions.

Synopsis of features and processes recorded within the interface domain

We interpret that the interface domain formed by replacement of the original zircon via ICDR reaction fronts that propagated into zircon (**Fig. 13**). The replacement process is epitaxial with the original zircon (Geisler et al., 2007) and is thus consistent with no observed misorientation across the grain. ICDR fronts are fluid-mediated; in some cases, the fluid is homogeneous throughout the lithology and may be derived from the partial breakdown of hydrous phases in metapelitic assemblages. In other cases, the fluid may be derived from the host mineral (endogenous fluids); these fluids would likely vary based on petrographic context such that minerals included in garnet may be subject to different composition fluids than grains hosted in the matrix. In the ICDR model, the rims of the original detrital zircon recrystallize in response to the propagation of the ICDR reaction front; a by-product of this reaction front is the removal of interstitial or relatively incompatible atoms (e.g., Al, radiogenic Pb) and precipitation of xenotime-rich zircon along planar features that are perhaps crystallographically controlled. Crystal defects (e.g., dislocations) and fractures promote reaction front propagation and thus progression of the reaction (Grand'homme et al., 2018). During exhumation, zircon crossed the chemical solvus and spinodal decomposition produced ellipsoidal features characterized by high concentrations of Y + P +Yb (+ Al) within previously enriched planar features.

Notably, high-resolution wavelength dispersive spectrometry maps of the zircon grain from the Goshen Dome locality indicate that the CL-dark band contains high concentrations of Th immediately against the unreacted core of the zircon (**Fig. 3**). A high-Th domain was not observed in the Rhodope samples and may indicate differences between the two localities in the process that initially produced the CL-dark domain. In both zircon grains, however, similarities in the planar features observed from the interface domains are consistent with fluid-mediated processes that modified the zircon.

Metamorphic events producing zircon rims

LASS-ICP-MS analyses (Peterman et al., 2016a) show that the rim domain of the Rhodope zircon is isotopically concordant, yields lower concentrations of minor and trace elements than the core, and has a flat HREE profile and a flat to negative Eu anomaly. Zircon rims that form in the presence of garnet commonly yield HREE-depleted profiles (e.g., Schaltegger et al., 1999; Rubatto, 2002; Hoskin and Schaltegger, 2003; Whitehouse and Platt, 2003) and strongly negative Eu anomalies are linked with crystallization in the presence of feldspar (Rubatto, 2002). The REE profile is consistent with formation during garnet-stability and the variability of the Eu anomaly suggests that feldspar may not have been present as a significant phase (no Eu anomaly) or may have been produced concurrently with the zircon rim (weak to strong Eu anomaly). We therefore interpret the rim to have formed during isothermal decompression from *UHP* conditions down to upper amphibolite facies at c. 150 to 145 Ma, consistent with interpretations of Krenn et al. (2010) and Liati et al. (2011).

Cross-cutting relationships between the rim and the interface domain indicate that the Rhodope rim formed after the interface-forming event. A surface area analysis of the core and rim domains within this grain using CL images suggests that nearly triple the Zr of the core would be required to produce these rims, which is unlikely to be available in subsolidus metapelitic systems, but can occur in the presence of melt (Kohn et al., 2015; Kohn and Kelly, 2018). Although the rocks at Xanthi exhibit evidence of local partial melting post-eclogite facies (Krenn et al., 2010; Liati et al., 2011), the garnet-kyanite metapelites exhibit minimal evidence of melting (Liati et al., 2011). We therefore suggest two possible mechanisms for rim formation. The convolute to blurred zoning could have formed via zircon recrystallization (ICDR) during exhumation from *UHP* to amphibolite facies conditions. In this explanation, the inward propagation of the recrystallization front produced an irregular, curved boundary against the core (or interface domain) and geochemically and isotopically reset the zircon (**Fig. 13**). The inward extent of this overprinting reaction can explain the discontinuous nature of the interface domain and why the interface domain disappears entirely in the center of this grain (**Fig. 2**) and elsewhere in other grains (e.g., 57074_1_z13; **Fig. 1**). However, recrystallization is normally accommodated by a fluid (Geisler et al., 2007; Rubatto, 2017) and the grain lacks evidence of fluid pathways (e.g., nano- or micropores). It is possible that porosity was transient or that the pores closed because of the conditions of metamorphism (e.g., Harlov et al., 2011; Ague and Axler, 2016). Alternatively, the margin of the grain, including the interface domain, may have partially dissolved in the presence of melt during exhumation and, upon melt crystallization, the rim grew at amphibolite facies conditions. Although the latter mechanism for rim formation explains the large volumes and geochemical attributes of the rim, it does not explain why some zircon grains retain faint evidence of original zoning in the rims (57074_1_z13; **Fig. 1**) whereas other rims have convolute, patchy zoning (57081X_z04, 57082_z04; **Fig. 1**), including the analyzed grain (**Fig. 2**).

In the Goshen Dome grain, the rim truncates both the interface domain and the filled fractures and is compositionally distinct from the filled fractures (**Fig. 3**). These attributes indicate that the rim postdates the interface-forming event and that, as with the Rhodope grain, the event

that formed the outermost rim locally recrystallized portions of the interface domain. The rim is too narrow on this grain to measure via LASS, but other grains from this sample indicate a range of REE profiles, including steep or flat HREE, flat or negative Eu anomaly, and, in some grains, an absent Ce anomaly. Although there are insufficient data to determine the precise conditions of metamorphism that produced this rim, the simplest explanation is that the rim-forming metamorphic event postdates the interface-forming event and occurred in response to different conditions from the interface-forming event.

Implications

Mobility of U and Pb can have significant implications for interpreting dates measured from zircon. Uranium is relatively immobile in zircon because it remains crystallographically bound, whereas Pb mobility is significantly more common (e.g., Cherniak and Watson, 2003; Cherniak, 2010) and often occurs in response to changes in temperature and/or the presence of fluids (Kogawa et al., 2012). The difference in relative mobility between U and Pb remains true for these samples: the core of the Rhodope grain lost >75% of the radiogenic Pb calculated to have accumulated prior to the metamorphic event that formed the interface domain while U remained immobile, as inferred from its homogeneous distribution throughout the detrital core, despite radiation damage. Within the interface domain, however, U is concentrated along planar defects and dislocations. If U had migrated to these defects during initial growth, we would expect to observe U features within the core. The lack of these features in the core suggests that the mechanism(s) responsible for mobilizing U did not occur while the dislocation loops were forming and migrating. Instead, the spatial restriction of U-decorated features within the interface domain suggests that U migrated to these defects during the interface-forming event and preserved those defects. Mobility of U during this event would likely have been fluid-assisted, but we note that the zircon lacks evidence of fluid pathways (e.g., nanoporosity). We therefore suggest that evidence of fluid pathways was eradicated by subsequent reaction at very-high-grade conditions. In contrast with U, Pb was mobile during multiple metamorphic events. The discordance measured in the core therefore represents the mixing of discrete Pb reservoirs that reflect evolving isotopic compositions at specific times in the zircon's history. Analysis of these different reservoirs by atom probe provides new temporal constraints on the *P*-*T*-t evolution of the host rock. Meaningful ages can be extracted from metamorphosed zircon—including the interface domain—but the correct interpretation of U-Pb isotopic data requires contextualization with the geologic history and may benefit from nanoscale analysis.

The assemblage of trace elements found in each type of nanoscale features can be correlated with the mechanisms driving their formation and used to effectively fingerprint the types of metamorphic processes operating at the atomic scale. The Pb clusters in the Rhodope grain are best explained by the migration and accumulation of Pb in dislocation loops in response to the annealing of radiation damage that we interpret occurred during the early stages of prograde metamorphism (**Fig. 13**). The planar features are restricted to the interface domain and are interpreted to have formed in response to ICDR-induced modification of zircon along a high d*P*/d*T* trajectory. Because of the lack of Pb clusters within the interface domain, we interpret

that it formed following Pb migration into dislocation loops and may also explain the lack of Pb clusters in the recrystallized rim. The distribution of nanoscale ellipsoidal features within the planar features suggests that their formation was driven by spinodal decomposition during exhumation. As the zircon passed the solvus, planar features with high enough concentrations of xenotime component were within the spinodal region; to minimize the Gibbs free energy, local equilibria favored nm-scale spinodal decomposition to produce high-Y + P zircon and low-Y + P zircon. The differences in charges among the cations in zircon and xenotime suggest that some charge balancing atoms should be expected to accompany and/or participate in the reactions that drive phase separation, thereby explaining why Al is present in many of these features. Because the compositions of these features depend in part on the parent zircon composition and the *P-T* path, it is possible that analysis of compositional heterogeneities among these ellipsoidal features may provide some constraints on the *P-T* history during exhumation.

Relatively few zircon grains display the atypical interface domain we describe, suggesting that it may form in either a narrow range of bulk compositions or along a limited set of metamorphic conditions. Lithologies that host zircon with atypical interface domains are mostly metapelites, including pelitic and restitic schists (Zeck and Williams, 2002; Taylor et al., 2015; Laurent et al., 2018). Some examples are found within granulites from kimberlite terranes (Schmitz and Bowring, 2004) and *HP* granitoids (Tomaschek, 2010). We are unaware of examples of the atypical interface domain in mafic to ultramafic compositions, but these bulk compositions typically have low zircon abundances and do not typically preserve inherited or detrital zircon grains on which metamorphic rims grow (e.g., Hoskin and Schaltegger, 2003). Although not exhaustive, the atypical interface domain can be found in a number of rock types, and thus it is unlikely that process responsible for producing this domain is narrowly restricted by composition. Instead, all of the above lithologies were metamorphosed at rather extreme metamorphic conditions: *HP*, *UHP,* and *UHT* conditions. Considering that the atypical domain contains high concentrations of xenotime component and the solubility of xenotime within zircon decreases with increasing *P*, we tentatively suggest that both the initial mol. % xenotime within zircon, and the *P-T* path of the lithology, drive the ICDR recrystallization process. Formation of the atypical interface requires enough xenotime component in the parent zircon to chemically drive local decomposition along a very-high-grade path (*HP, UHP,* or *UHT*). The preservation of the interface domain is likely determined by the exhumation and fluid history of the rock during subsequent geologic events. In cases where the host rock resides or stalls at middle- to lower-crust conditions, the zircon will presumably thermally equilibrate or react with fluids, which could drive recrystallization of the rims and thus (partially) overprint the atypical interface domain. The presence of the atypical interface domain is significant because it preserves aspects of both the prograde and retrograde response of zircon to metamorphism at *HP*, *UHP,* and *UHT* conditions.

Crustal metamorphism gives rise to a range of processes in zircon (often unrecognized) that may be responsible for trace element modification and therefore can provide new insights into the geological (*P-T*-t) history of the host rock. Because of the widespread use of zircon as a

monitor of crustal evolution and geochronometer, it is important to consider the implications of trace element mobility on the record of metamorphism extracted from zircon. Our findings suggest three key implications: (1) Whereas Pb was mobile during multiple metamorphic events, U mobility was only documented within the interface domain and thus only one metamorphic event. Discrete Pb reservoirs within zircon reflect evolving isotopic compositions at specific times in the zircon's history; analysis by atom probe can provide new temporal constraints on the *P*-*T*-t evolution of the host rock. (2) Trace element migration and clustering occurs in response to multiple mechanisms; the assemblage of trace elements, morphology of the features, and spatial distribution within the zircon reflect the mechanism(s) that induced migration. (3) The exclusive presence of the atypical interface domain in zircon from very-high-grade metamorphic lithologies suggests that these features may reflect a high-grade *P*-*T* path.

Acknowledgements

The authors thank D. Rubatto for editorial handling. Two anonymous reviewers provided helpful comments that improved the manuscript. This work was supported in part by NSF EAR-1650054 to Peterman and Bowdoin College Research Funds. The SEM facility at Bowdoin was supported by NSF MRI-1530963 to E.M. Peterman and R.J. Beane. The Atom Probe Facility is supported by ARC CE11E0070 and SIEF RI13-01 to S.M. Reddy. The Advanced Resource Characterisation Facility under the auspices of the National Resource Sciences Precinct—a collaboration between the Commonwealth Scientific and Industrial Research Organization, Curtin University, and the University of Western Australia—was supported by the Science and Industry Endowment Fund. The UltraChron development project was supported by NSF EAR-0004077 and NSF EAR-0549639 to M.L. Williams and M.J. Jercinovic at the University of Massachusetts, and collaboratively by CAMECA. The authors declare that they have no conflict of interest.

Figure Captions

Figure 1: Representative CL images of zircon from the Rhodope Metamorphic Complex. Images in grayscale collected with a panchromatic CL detector; color images collected with a Tescan Rainbow CL detector. Dotted pink lines mark boundary between core domains and CL-dark portion of the interface domain; dotted yellow lines mark the boundary between the CL-bright portion of the interface domain and the rim. White dotted lines mark boundaries within core or rim domains. All scale bars are 20 μm.

Figure 2: Rhodope zircon grain. (A) Panchromatic CL image. Dotted pink lines mark boundary between the core and CL-dark portion of the interface domain; dotted yellow lines mark the boundary between the CL-bright portion of the interface domain and the rim. White dotted line marks outer boundary of the rim. The portion of the rim adjacent to the interface domain has complex variation in CL whereas the outer portion of the rim has a lower intensity, more homogeneous CL signal. Red dashed circles denote locations of laser ablation split stream

(LASS) ICP-MS analyses. Locations of atom probe specimens that ran successfully shown as filled circles; open circle did not run. Yellow box marks location of TEM foil. Blue box marks the area shown in the inset of the Y concentration map (B) produced via time-of-flight (ToF)-SIMS. (C) Blue dashed lines mark locations of healed fractures within the core. (D) BSE image of the same grain shows oscillatory zoning; healed fractures are bright. Dark spots are inclusions and pits in the sample surface. (E) Pole figure showing the orientations of the {100} and {001} planes (purple) and the orientation of atom probe specimens (white dot).

Figure 3: Panchromatic CL image of zircon from the Goshen Dome. White dotted lines mark boundaries within the core. Pink dotted lines mark boundary between the core and the CL-dark portion of the interface domain. Yellow dotted lines mark the boundary between the CL-bright portion of the interface domain and the rim. EPMA maps (modified from Peterman et al., 2016b) indicate compositional differences among the domains (see text). BSE map (pre-LASS analysis) distinguishes fractures and inclusions (black) from coherent zircon (grayscale). EBSD map is a composite of band contrast (grayscale) + misorientation with respect to position marked by white dot; see color scale) + grain boundaries (red = 2–10°, black > 10°). Blue arrows indicate the filled fracture and pink arrows mark an example CL-dark portion within the interface domain; the same fracture and CL-dark domain are indicated in CL, EPMA, BSE, and EBSD maps.

Figure 4: Representative spectra from atom probe analysis; colors mark ranges used in reconstructions.

Figure 5: Reconstructions of specimens from the Rhodope zircon. **(A)** Rim domain exhibits homogeneous distributions of Y + U (other elements are also homogeneous; not shown for simplicity) (M8). **(B)** The CL-bright portion of the interface (M7) is lower-U than the rim, corresponding to its higher CL emission. **(C-E)** Core specimens (M15–M17) contain high concentrations of Pb ± Y; other elements are homogeneously distributed. **(F)** Close-up of two of the Pb + Y clusters from **E**; this reconstruction includes only Pb + Y atoms.

Figure 6: Reconstructions of specimen M6, CL-dark portion of the interface domain, Rhodope zircon. **(A, B)** Annotated reconstructions of Y. Planar features with high concentrations marked as I–IV; planar features with low concentrations marked as 1–4. Feature 2 cross-cuts Features 1 and IV. **(C)** Annotated reconstruction of Y + U with high-U domains marked in blue. Curviplanar high-U domain partially overlaps low-Y Feature 4. **(D)** Reconstruction of Yb. High-Yb correlates with high-Y Features I–IV, but low-Yb domains are not resolvable due to signal-to-noise.

Figure 7: Reconstructions of Y, U, P, and Yb from specimen M12, CL-dark portion of the interface domain, Rhodope zircon. Blue lines mark high-U features; black arrows indicate clusters within the high-Y features that contain higher concentrations of Y + P + Yb.

Figure 8: Reconstructions of P, Y, U, and Pb from specimen M13, CL-dark portion of the interface domain, Rhodope zircon. All reconstructions shown at the same rotation. Y and P yield similar features; Y has more favorable signal-to-noise. The top and bottom of the specimen are lower in Y and P than the central domain, which contains complex cross-cutting features of high and low concentrations. Feature 1 is a planar feature with high U + Y + P. Feature 2 is a high-U linear feature, similar to the feature identified in **Fig. 5**. Feature 3 is a low-Y + P planar feature. Ellipsoidal features with very-high concentrations of Y + P are located in the central portion of the specimen; they are not co-located with high-U features. Pb shows no clusters and no domains of high (or low) concentration, but compositional analysis (Table 3) indicates Pb above background within the ellipsoidal features.

Figure 9: Composite reconstruction of U + Y + PO_3 + Al +Yb + Pb; single element reconstructions U; Y; PO_3; Yb; Al; and Pb. All reconstructions shown at the same orientation. U domains do not spatially correlate with other trace elements. Y correlates with PO_3 + Yb; Al correlates in some locations (black arrows) and does not in others (blue arrows). Black dashed lines mark regions of low trace element concentrations.

Figure 10: Reconstructions of the CL-dark portion of the interface domain within the Goshen Dome zircon. **a)** Y from specimen M14. Specimen exhibits parallel planar features that vary in Y concentration within a high-Y feature. An undulating margin bounds the high- and low-Y features (dashed line) and the low-Y feature contains a high-Y linear feature. **b)** Phosphorous and **c)** yttrium exhibit planar features of high- and low-concentrations. Within the high-Y feature, clusters are further enriched in Y, as shown in a close-up in **d.** For visual clarity, **c** and **d** are 20 nm thick slices of the full reconstruction. **e)** A volume rendering of Y concentration shows high- and low-Y planar features within the high-Y feature. Red indicates highest concentrations for this color ramp. **b–e** from specimen M15.

Figure 11: TEM images from the core of the zircon. White arrows denote dislocation loops. **a**) BF-STEM image. **b**) Higher magnification BF-STEM image showing toroidal dislocation loops, the smallest of which measures c. 10 nm. **c**) HAADF image from the zircon core. **d**) EDS map of Pb distribution from the region imaged in **c** showing the spatial correlation between bright spots in the HAADF image and high Pb concentration.

Figure 12: Model for xenotime-zircon solid solution, modified from Tomaschek, 2010. **a)** Zircon-xenotime miscibility varies as a function of temperature, mol. % xenotime, and pressure. Curves modified from Tomaschek (2010). **b)** Schematic representation of the change in the Gibbs free energy; colors correspond to the pressure-dependent curves shown in A. Dotted lines show the inflection point on each curve; if the mol. % xnt in zircon increased beyond this value, the negative curvature in Gibbs free energy would induce spinodal decomposition.

Figure 13: Schematic model for producing observed textures.; numbers correspond to schematic *P-T* diagram, modified from Kohn et al. (2015); dashed Rhodope P-T path adapted from Krenn et al. (2010); dotted path is inferred. **1)** Initial crystallization characterized by oscillatory zoning.

2) Radiation damage accumulates. **3)** Metamorphism begins. As T increases, radiation damage anneals and induces formation of dislocation loops; Pb caught in migrating loops (green spheres). **4)** Interface-coupled dissolution-reprecipitation (ICRD) mediated by metamorphic fluids propagates from the edge of the grain towards the core. ICDR front identified by CL-dark domain (black), which is high in U + Y + P + Yb (+ Al). CL-bright domain (blue) is the U + Y + P poor rim produced as the ICDR front propagated into the grain. Lower panel is a schematic cross-section through the red box showing a vertical view of the cross-cutting features (purple) produced within the CL-dark domain. **5)** Upon decompression from peak conditions, sample crosses the solvus. Features previously enriched in Y + P + Yb (+ Al) undergo spinodal decomposition to form the ellipsoidal clumps (orange) within the high-Y + P + Yb (+ Al) planar domains (purple). **6)** Rim re-equilibrates with the new matrix; cuspate boundary of the CL-bright domain produced by the farthest extent of the re-equilibration reaction front. Additional new growth of zircon may occur.

References cited

Ague, J.J., and Axler, J.A., 2016, Interface coupled dissolution-reprecipitation in garnet from subducted granulites and ultrahigh-pressure rocks revealed by phosphorous, sodium, and titanium zonation. American Mineralogist, 101, p. 1696-1699.

Armstrong, T.R., Tracy, R.J., and Hames, W.E. (1992) Contrasting styles of Taconian, Eastern Acadian and Western Acadian metamorphism, central and western New England. Journal of Metamorphic Geology, 10, 415–426, doi:10.1111/j.1525-1314.1992.tb00093.x.

Bursill, L. A. and McLaren, A. C. (1966) Transmission electron microscope study of natural radiation damage in zircon (ZrSiO4). Phys. Status Solidi B 13, 331–343.

Cheney, J.T., Spear, F.S., and Kirk-Lawlor, N. (2006) The mysterious machinations of muscovite and monazite during metamorphism or How the CVS (Connecticut Valley synclinorium) survived PMS (post-metamorphic-stretching). Geological Society of America Abstracts with Programs, 38, 49, https://gsa.confex.com/gsa/2006AM/finalprogram/abstract_113956.htm.

Cherniak, D.J., Lanford, W.A., and Ryerson, F.J., 1991, Lead diffusion in apatite and zircon using ion implantation and Rutherford Backscattering techniques. Geochimica et Cosmochimica Acta, v. 55, issue 6, p. 1663 – 1673.

Cherniak, D.J. and Watson, E.B., 2003, Diffusion in Zircon, In: Zircon, ch. 5, pp. 113-143 (*Reviews in Mineralogy and Geochemistry*, vol. 53, J.M. Hanchar and P.W.O. Hoskin, Eds.), Mineralogical Society of America, Washington D.C.

Cherniak, D.J., 2010, Diffusion in accessory minerals: zircon, titanite, apatite, monazite and xenotime. Reviews in Mineralogy and Geochemistry, v. 72, issue 1, pp. 827 – 869.

Coleman, D.S., Gray, W., and Glazner, A.F., 2004, Rethinking the emplacement and evolution of zoned plutons: Geochronologic evidence for incremental assembly of the Tuolumne Intrusive Suite, California. Geology, v. 32, no. 5, p 433 – 436. doi: 10.1130/G20220.1;

Corfu, F., Hanchar, J.M., Hoskin, P.W.O., and Kinny, P., 2003, Atlas of zircon textures. Reviews in Mineralogy and Geochemistry, 53 (1), 469-500. Doi: 10.2113/0530469

Degeling, H., Eggins, S., and Ellis, D.J. (2001) Zr budgets for metamorphic reactions, and the formation of zircon from garnet breakdown. Mineralogical Magazine, 65, 749–758, doi:10.1180/0026461016560006.

Devaraj, A., Colby, R., Vurpillot, F., Thevuthasan, S., 2014, Understanding atom probe tomography of oxide-supported metal nanoparticles by correlation with atomic-resolution electron microscopy and field evaporation simulation. Journal of Physical Chemistry Letters, v. 5, no. 8, pp. 1361 – 1367.

Ewing, R.C., Meldrum, A., Wang, L., Weber, W.J., and Corrales, L.R., 2003, Radiation effects in zircon. Reviews in Mineralogy and Geochemistry, v. 53, no. 1, pp. 387-425. https://doi.org/10.2113/0530387

Fougerouse, D., Reddy, S. M., Saxey, D. W., Rickard, W. D. A., van Riessen, A., & Micklethwaite, S. (2016). Nanoscale gold clusters in arsenopyrite controlled by growth rate not concentration: Evidence from atom probe microscopy. American Mineralogist, *101*(8), 1916–1919. doi.org/10.2138/am-2016-5781

Fougerouse, D., Reddy, S.M., Saxey, D.W., Erickson, T.M., Kirkland, C.L., Rickard, W.D.A., Seydoux-Guillaume, A.M., Clark, C., and Buick, I.S. (2018) Nanoscale distribution of Pb in monazite revealed by atom probe microscopy. Chemical Geology, 479, 251-258.

Fougerouse, D., Reddy, S.M., Kirkland, C.L., Saxey, D.W., Rickard, W.D., and Hough, R.M. (2019) Time-resolved, defect-hosted, trace element mobility in deformed Witwatersrand pyrite. Geoscience Frontiers, 10(1), 55-63.

Fynn, G. W. and Powell, W.J.A. (1979) The Cutting and Polishing of Electro-optic Materials. Adams Hilger, London, pp 216.

Garver, J.I., Brandon, M.T., Roden-Tice, M.K., and Kamp, P.J.J., 1999, Exhumation history of orogenic highlands determined by detrital fission track thermochronology. *In* Ring, U., Brandon, M.T., Willet, S.D., and Lister, G.S. (eds) Exhumation processes: normal faulting, ductile flow. Geological Society of London Special Publications, v. 154, pp. 283-304.

Gatewood, M.P., Dragovic, B., Stowell, H.H., Baxter, E.F., Hirsch, D.M., and Bloom, R. (2015) Evaluating chemical equilibration in metamorphic rocks us- ing major element and Sm-Nd isotopic age zoning in garnet, Townshend Dam, Vermont, U.S.A. Chemical Geology, 401, 151–168, http://dx.doi.org/10.1016/j. chemgeo.2015.02.017.

Gebauer, D. (1993) in Pre-Mesozoic Geology in the Alps, J. F. v. Raumer, F. Neubauer, Eds. Springer, Berlin, pp. 93–117.

Gehrels, G.E., Blakey, R., Karlstrom, K.E., Timmons, J.M., Dickinson, B., and Pecha, M., 2011, Detrital zircon U-Pb geochronology of Paleozoic strata in the Grand Canyon, Arizona. Lithosphere, v. 3, no. 3, p. 183-200. doi: 10.1130/L121.1

Geisler, T., Schaltegger, U., and Tomaschek, F. (2007) Re-equilibration of zircon in aqueous fluids and melts. Elements, 3, 43–50, doi:10.2113/gselements.3.1.43.

Geisler, T., Pidgeon, R.T., van Bronswijk, W., and Pleysier, R., 2001, Kinetics of thermal recovery and recrystallization of partially metamict zircon: a Raman spectroscopic study. European Journal of Mineralogy, v. 13, 1163-1176.

Geisler, T., 2002, Isothermal annealing of partially metamict zircon: evidence for a three-stage recovery process. Physics and Chemistry of Minerals, v. 29, issue 6, p. 420 – 429.

Geisler, T., Pidgeon, R.T., Kurtz, R., van Bronswijk, W., and Schleicher, H., 2003, Experimental hydrothermal alteration of partially metamict zircon. American Mineralogist, v. 88, p. 1496 – 1513.

Geisler, T., Janssen, A., Scheiter, D., Stephan, T., Berndt, J., and Putnis, A., 2010, Aqueous corrosion of borosilicate class under acidic conditions: a new corrosion mechanism. Journal of Non-Crystalline Solids, v. 356, p 1458-1465.

Grand'Homme A., Janots E., Seydoux-Guillaume A.M., Guillaume D., Magnin V., Hövelmann J., Höschen C., and Boiron M.C. (2018). Mass transport and fractionation during monazite alteration by anisotropic replacement. Chemical Geology, 484, 51-68.

Gray, M.B. and Zeitler, P.K., 1997, Comparison of clastic wedge provenance in the Appalachian foreland using U/Pb ages of detrital zircons. Tectonics, v. 16, issue 1. https://doi.org/10.1029/96TC02911

Hanchar, J.M., Finch, R.J., Hoskin, P.W.O., Watson, E.B., Cherniak, D.J., and Mariano, A.N., 2001, Rare earth elements in synthetic zircon: Part 1. Synthesis, and rare earth element and phosphorus doping. American Mineralogist, v. 86, p. 667-680.

Hanchar, J.M. and Miller, C.F., 1993, Zircon zonation patterns as reealed by cathodoluminescence and backscattered electron images: Implications for interpretation of complex crustal histories. Chemical Geology, 110, 1-13.

Harley, S.L., Kelly, N.M., and Möller, A. (2007) Zircon behavior and the thermal histories of mountain chains. Elements, 3, 25–30, doi:10.2113/gselements.3.1.25.

Harlov, D.E., Wirth, R., and Hetherington, C.J. (2011) Fluid-mediated partial alteration in monazite: the role of coupled dissolution–reprecipitation in element redistribution and mass transfer. Contributions to Mineralogy and Petrology, v. 162, p. 329-348. DOI 10.1007/s00410-010-0599-7

Hatch, N.L. Jr., and Warren, C.R. (1981) Geologic map of the Goshen quadrangle, Franklin and Hampshire Counties, Massachusetts. U.S. Geological Survey Geologic Quadrangle Map GQ-1561, scale 1: 24,000, http://pubs.er.usgs.gov/publication/gq1561.

Hellman, O.C., Vandenbroucke, J.A., Rüsing, J., Isheim, D., and Seidman, D.N. (2000) Analysis of three-dimensional atom-probe data by the proximity histogram. Microscopy and Microanalysis, 6(05), 437-444.

Hermann, J. and Rubatto, D., 2003, Relating zircon and monazite domains to garnet growth zones: age and duration of granulite facies metamorphism in the Val Malenco lower crust. Tectonics, v. 21, issue 9. https://doi.org/10.1046/j.1525-1314.2003.00484.x

Hoskin, P.W.O., and Ireland, T.R. (2000) Rare earth element chemistry of zircon and its use as a provenance indicator. Geology, 28, 627–630.

Hoskin, P.W.O., and Schaltegger, U. (2003) The composition of zircon and igneous and metamorphic petrogenesis. Reviews in Mineralogy and Geochemistry, 53, 27–62.

Janák, M., Froitzheim, N., Georgiev, N., Nagel, T.J., and Sarov, S., 2011, P-T evolution of kyanite eclogite from the Pirin Mountains (SW Bulgaria): Implications for the Rhodope UHP Metamorphic Complex. J. Metamorph. Geol. 29, 317–332.

Karabinos, P., Samson, S.D., Hepburn, J.C., and Stoll, H.M. (1998) Taconian Orogeny in the New England Appalachians; collision between Laurentia and the Shelburne Falls Arc. Geology, 26, 215–218.

Kirchenbaur, M., Pleuger, J., Jahn-Awe, S., Nagel, T.J., Froitzheim, N., Fonseca, R.O.C., and Münker, C., 2011, Timing of high-pressure metamorphic events in the Bulgarian Rhodopes from Lu–Hf garnet geochronology. Contrib. Mineral. Petrol. 163, 897–921.

Kirkland, C.L., Fougerouse, D., Reddy, S.M., Hollis, J., and Saxey, D.W. (2018) Assessing the mechanisms of common Pb incorporation into titanite. Chemical Geology, 483, 558-566.

Klapper, H., 2010, Generation and propagation of defects during crystal growth. Springer Handbook of Crystal Growth, p. 93-132.

Kohn, M.J., Corrie, S.L., and Markley, C., 2015, The fall and rise of metamorphic zircon. American Mineralogist, v. 100, p. 897-908.

Kohn, M.J., and Kelly, N.M. (2018) Petrology and geochronology of metamorphic zircon. *In* Moser, D.E., Corfu, F., Darling, J.R., Reddy, S.M., and Tait, K. (eds) Microstructural Geochronology: Planetary Records Down to Atom Scale, v. 232, p. 35-61. https://doi.org/10.1002/9781119227250.ch2

Kogawa, M., Watson, E.B., Ewing, R.C., and Utsunomiya, S. (2012) Lead in zircon at the atomic scale. American Mineralogist, v. 97, p. 1094–1102 (2012).

Krenn, K., Bauer, C., Proyer, A., Klötzli, U., and Hoinkes, G., 2010, Tectonometamorphic evolution of the Rhodope orogen. Tectonics 29, TC4001.

Kusiak, M.A., Whitehouse, M.J., Wilde, S.A., Nemchin, A., and Clark, C., 2013, Mobilization of radiogenic Pb in zircon revealed by ion imaging: Implications for early Earth geochronology. Geology, 41 (3), 291-294.

Kusiak MA, Dunkley DJ, Wirth R, Whitehouse MJ, Wilde SA, Marquardt K (2015) Metallic lead nanospheres discovered in ancient zircons. Proc Nat Acad Sci 112:4958-4963. https://doi.org/10.1073/pnas.1415264112

Kusiak, M.K., Wilde, S.A., Wirth, R., Whitehouse, M.J., Dunkley, D.J., Lyon, I., Reddy, S.M., Berry, A., and de JOnge, M., 2018, Detecting micro-and nanoscale variations in element mobility in high-grade metamorphic rocks: implication for precise U-Pb dating of zircon. *In* Moser, D.E., Corfu, F., Darling, J.R., Reddy, S.M., and Tait, K. (eds) Microstructural Geochronology: Planetary Records Down to Atom Scale, v. 232, p. 279-291.

La Fontaine, A., Piazolo, S., Trimby, P., Yang, L., and Cairney, J.M., 2017, Laser-Assisted atom probe tomography of deformed minerals: A zircon case study. Microscopy and Microanalysis, v. 23, 404-413. doi:10.1017/S1431927616012745.

Laurent A.T., Bingen B., Duchene S., Whitehouse M.J., Seydoux-Guillaume A-M, and Bosse V. (2018). Decoding protracted zircon geochronological record in ultra-high temperature granulite, and persistence of partial melting in the crust, Rogaland, Norway. Contrib Mineral Petrol, 173: 29. https://doi.org/10.1007/s00410-018-1455-4

Liati, A., 2005, Identification of repeated Alpine (ultra) high-pressure metamorphic events by U–Pb SHRIMP geochronology and REE geochemistry of zircon: The Rhodope zone of Northern Greece. Contrib. Mineral. Petrol. 150, 608–630.

Liati, A., Gebauer, D., and Fanning, C.M., 2011, Ultrahigh- Pressure Metamorphism: 25 Years after the Discovery of Coesite and Diamond, in L. Dobrzhinetskaya, S. W. Garyad, S. Wallis, S. Cuthbert, Eds. Elsevier, London, pp. 295–324.

Liati, A., Theye, T., Fanning, C.M., Gebauer, D., and Rayner, N., 2016, Multiple subduction cycles in the Alpine orogeny, as recorded in single zircon crystals (Rhodope zone, Greece). Gondwana Research, v. 29, p. 199-207. http://dx.doi.org/10.1016/j.gr.2014.11.007

Macdonald, F.A., Ryan-Davis, J., Coish, R.A., Crowley, J.L, and Karabinos, P., 2014, A newly identified Gondwanan terrane in the northern Appalachian Mountains: Implications for the Taconic orogeny and closure of the Iapetus Ocean. Geology. doi:10.1130/G35659.1

Meldrum, A., Boatner, L.A., Weber, W.J., and Ewing, R.C.,1998, Radiation damage in zircon and monazite. Geochimica et Cosmochimica Acta, 62 (14), 2509-2520.

Melnik, O.E., and Bindeman, I.N., 2018, Modeling of trace element zoning patterns in accessory minerals with emphasis on the origin of micrometer-scale oscillatory zoning in zircon. American Mineralogist, v. 103, p. 355–368.

Mposkos, E. D., and Kostopoulos, D.K., 2001, Diamond, former coesite and supersilicic garnet in meta-sedimentary rocks from the Greek Rhodope: A new ultrahigh-pressure metamorphic province established. Earth Planet. Sci. Lett. 192, 497–506.

Murakami, T., Chakoumakos, B.C., Ewing, R.C., Lumpkin, G.R., and Weber, W.J., 1991, Alpha-decay event damage in zircon. American Mineralogist, v. 76, p. 1510-1532.

Nasdala L, Pidgeon RT, Wolf D, and Irmer G, 1998, Metamictization and U-Pb isotopic discordance in single zircons: a combined Raman microprobe and SHRIMP ion probe study. Mineralogy and Petrology, v. 62, issue 1-2, p. 1-27.

Nasdala, L., Wenzel, M., Vavr, G., Irmer, G., Wenzel, T., and Kober, B., 2001, Metamictization of natural zircon: accumulation versus thermal annealing of radioactivity-induced damage. Contributions to Mineralogy and Petrology, v. 141, p. 125-144. DOI 10.1007/s004100000235

Nasdala, L., Lengauer, CL, Hanchar, JM, Kronz, A, Wirth, R., Blanc, P., Kennedy, AK, Seydoux-Guillaume, A-M., 2002, Annealing radiation damage and the recovery of cathodoluminescence. Chemical Geology, v. 191, p. 121-140.

Nasdala, L., Reiners, P.W., Garver, JI, Kennedy, AK, Stern, RA, Balan, E., and Wirth, R., 2004, Incomplete retention of radiation damage in zircon from Sri Lanka. American Mineralogist, v. 89, p. 219-231.

Nemchin, A.A., Giannini, L.M., Bodorkos, A., and Oliver, N.H.S., 2001, Ostwald ripening as a possible mechanism for zircon overgrowth formation during anatexis: theoretical constraints, a numerical model, and its application to pelitic migmatites of the Tickalara Metamorphics, northwestern Australia. Geochimica et Cosmochimica Acta, v. 65, issue 16, p. 2771–2788. https://doi.org/10.1016/S0016-7037(01)00622-6

Perraki, M., A. Proyer, E. Mposkos, R. Kaindl, and G. Hoinkes (2006), Raman micro-spectroscopy on diamond, graphite and other carbon polymorphs from the ultrahigh-pressure metamorphic Kimi Complex of the Rhodope Metamorphic Province, NE Greece, Earth Planet. Sci. Lett., 241, 672– 685, doi:10.1016/j.epsl.2005.11.014.

Peterman, E.M., Reddy, S.M, Saxey, D.W., Snoeyenbos, D.R., Rickard, W.D.A., Fougerouse, D., and Kylander-Clark, A.R.C., 2016a, Nanogeochronology of discordant zircon measured by atom probe microscopy of Pb-enriched dislocation loops. *Science Advances,* v. 2, e:1601218. doi: 10.1126/sciadv.1601318

Peterman, E.M., Snoeyenbos, D.R., Jercinovic, M.J., and Kylander-Clark, A., 2016b, Dissolution-reprecipitation metasomatism and growth of zircon within phosphatic garnet in metapelites from western Massachusetts. *American Mineralogist,* v. 101, p. 1792-1806.

Peterman, E.M. and Snoeyenbos, D.R., 2015, Atypical dissolution-reprecipitation reactions in zircon from HP/UHP metapelites, *Geological Society of America Abstracts with Programs,* vol. 47, no. 7, p.168.

Piazolo, S., La Fontaine, A., Trimby, P., Harley, S., Yang, L., Armstrong, R., and Cairney, J.M., 2016, Deformation-induced trace element redistribution in zircon revealed using atom probe tomography. Nat. Commun. 7, 10490.

Pidgeon, R.T., 2014, Zircon radiation damage ages. Chemical Geology, v. 367, p. 13-22.

Putnis, A., 2002, Mineral replacement reactions: from macroscopic observations to microscopic mechanisms. Mineralogical Magazine, vol. 66(5), p. 689-708

Putnis, A., 2009, Mineral replacement reactions. Reviews in Mineralogy and Geochemistry, v. 70, no. 1, p. 87-124. https://doi.org/10.2138/rmg.2009.70.3

Putnis, A., and Austrheim, H. (2010) Fluid-induced processes: metasomatism and metamorphism. Geofluids, v. 10, p. 254-269. https://doi.org/10.1111/j.1468-8123.2010.00285.x

Putnis A., and John, T. (2010) Replacement processes in the Earth's Crust. Elements, v. 6, p. 159-164. doi:10.2113/gselements.6.3.159

Pyle, J.M., and Spear, F.S. (2003) Four generations of accessory-phase growth in low-pressure migmatites from SW New Hampshire. American Mineralogist, 88, 338–351.

Pyle, J.M., Spear, F.S., Cheney, J.T., and Layne, G. (2005) Monazite ages in the Chesham Pond Nappe, SW New Hampshire, U.S.A.: Implications for assembly of central New England thrust sheets. American Mineralogist, 90, 592–606.

Reddy, S.M., Timms, N.E., Trimby, P., Kinny, P.D., Buchan, C., and Blake, K., 2006, Crystal-plastic deformation of zircon: A defect in the assumption of chemical robustness. Geology, 34, 257–260.

Reddy, S.M., Timms, N.E., Pantleon, W., and Trimby, P., 2007, Quantitative characterization of plastic deformation of zircon and geologic implications. Contributions to Mineralogy and Petrology, 153 (6), 625-645.

Reddy, S.M., Timms, N.E., Hamilton, P.J., and Smyth, H.R., 2009, Deformation-related microstructures in magmatic

zircon and implications for diffusion. Contributions to Mineralogy and Petrology, v. 157, issue 2, p. 231-244.

Reddy, S.M., Johnson, T.E., Fischer, S., Rickard, W.D.A., and Taylor, R.J.M., 2015, Precambrian reidite discovered in shocked zircon from the Stac Fada impactite, Scotland. Geology, v. 43, no. 10, p. 899-902. https://doi.org/10.1130/G37066.1

Reddy, S.M., van Riessen, A., Saxey, D.W., Johnson, T.E., Rickard, W.D.A., Fougerouse, D., Fischer, S., Prosa, T.J., Rice, K.P., Reinhard, D.A., Chen, Y., and Olson, D., 2016, Mechanisms of deformation-induced trace element migration in zircon resolved by atom probe and correlative microscopy. Geochimica et Cosmochimica Acta, v. 195, p. 158-170. https://doi.org/10.1016/j.gca.2016.09.019

Reischmann, T., and Kostopoulos, D., 2002, Timing of UHPM in metasediments from the Rhodope Massif, N Greece. Geochim. Cosmochim. Acta 66 (Suppl. 1), 633.

Rubatto, D. (2002) Zircon trace element geochemistry: Partitioning with garnet and the link between U–Pb ages and metamorphism. Chemical Geology, 184, 1, 123–138, doi:10.1016/S0009-2541(01)00355-2.

Rubatto, D., Muntener, O., Barnhoorn, A., and Gregory, C. (2008) Dissolution- reprecipitation of zircon at low-temperature, high-pressure conditions (Lanzo Massif, Italy). American Mineralogist, 93, 1519–1529.

Rubatto, D., 2017, Zircon: the metamorphic mineral. Reviews in Mineralogy and Geochemistry 83: 261-296.

Salje., E.K.H., Chrosch, J., and Ewing, R.C., 1999, Is "metamictization" of zircon a phase transition? American Mineralogist, 84, 1107-1116.

Saxey, D., Reddy, S.M., Fougerouse, D., and Rickard, W.D. (2018) The Optimization of Zircon Analyses by Laser-Assisted Atom Probe Microscopy: Insights from the 91500 Zircon Standard. Microstructural Geochronology: Planetary Records Down to Atom Scale, 293-313.

Schaltegger, U., Fanning, C., Günther, D. et al. (1999) Growth, annealing and recrystallization of zircon and preservation of monazite in high-grade metamorphism: conventional and in-situ U-Pb isotope, cathodoluminescence and microchemical evidence. Contributions to Mineralogy and Petrology, v. 134: 186-201. https://doi.org/10.1007/s004100050478

Schmidt, S., Nagel, T.J., and Froitzheim, N., 2010, A new occurrence of microdiamond-bearing metamorphic rocks, SW Rhodopes, Greece. Eur. J. Mineral. 22, 189–198.

Schoene, B., Samperton, K.M., Eddy, M.P., Keller, G., Adatte, T., Bowring, S.A., Khadri, S.F.R., and Gertsch, B., 2015 U-Pb geochronology of the Deccan Traps and relation to the end-Cretaceous mass extinction. Science: 347; 6218, p. 182-184. 10.1126/science.aaa0118

Schmitz, M.D., and Bowring, S.A., 2004, Lower crustal granulite formation during Mesoproterozoic Namaqua-Natal collisional orogenesis, southern Africa. South African Journal of Geology, v. 107, p. 19-42.

Seydoux-Guillaume, A.M., Bingen, B., Paquette, J.L., and Bosse, V. (2015). Nanoscale evidence for uranium mobility in zircon and the discordance of U-Pb chronometers. Earth and Planetary Science Letters, v. 409, p. 43-48.

Seydoux-Guillaume, A-M., Bingen, B., Bosse, V., Janots, E., and Laurent, A.T., 2018, Transmission electron microscope imaging sharpens geochronological interpretations of zircon and monazite. *In* Moser, D.E., Corfu, F., Darling, J.R., Reddy, S.M., and Tait, K. (eds) Microstructural Geochronology: Planetary Records Down to Atom Scale, v. 232, p. 261-275. https://doi.org/10.1002/9781119227250.ch12

Seydoux-Guillaume, A.-M., Fougerouse, D., Laurent, A., Gardés, E., Reddy, S., and Saxey, D. (2019) Nanoscale resetting of the Th/Pb system in an isotopically-closed monazite grain: A combined atom probe and transmission electron microscopy study. Geoscience Frontiers, 10(1), 65-76.

Snoeyenbos, D.R., Koziol, A., Russell, A., Ebel, D.S., and Valley, J.W. (2011) Prograde growth history of possible relic UHP garnets from the Taconian of Western Massachusetts. American Geophysical Union, Fall Meeting 2011, Abstract V21G-04.

Soman, A., Geisler, T., Tomaschek, F., Grange, M., and Berndt, J., 2010, Alteration of crystalline zircon solid solutions: a case study on zircon from an alkaline pegmatite from Zomba–Malosa, Malawi. Contributions to Mineralogy and Petrology, 160, p. 909-930.

Spencer, C.J., Kirkland, C.L., and Taylor, R.J.M. (2016) Strategies towards statistically robust interpretations of *in situ* U – Pb zircon geochronology. Geoscience Frontiers, p. 581-589. http://dx.doi.org/10.1016/j.gsf.2015.11.006

Taylor, R.J.M., Clark, C., Johnson, T.E., Santosh, M., and Collins, A.S., 2015, Unravelling the complexities in high-grade rocks using multiple techniques: the Achankovil Zone of southern India. Contributions to Mineralogy and Petrology, v. 169:51. DOI 10.1007/s00410-015-1147-2

Thompson, K., Lawrence, D., Larson, D.J., Olson, J. D., Kelly, T. F., and Gorman, B., 2007, In situ site-specific specimen preparation for atom probe tomography. Ultramicroscopy 107, 131–139.

Timms, N.E., Reddy, S.M., Fitz Gerald, J.D., Green, L., and Muhling, J.R.., 2012. Inclusion-localised crystal-plasticity, dynamic porosity, and fast-diffusion pathway generation in zircon. Journal of Structural Geology 35, 78-89

Tomaschek, F., 2010, Praktische Aspekte der Mischkristallphase Zirkon: Reequilibrierungsprozess, Zirkon-Xenotim Mischungslücke, geochronologische Anwendungen in einem polymetamorphen Kristallinkomplex (Syros, Kykladen, Griechenland). Ph.D. thesis, Münster, Westfälische Wilhelms-Universität Münster, pp. 431.

Tomaschek, F., Kennedy, A.K., Villa, I.M., Lagos, M., and Ballhaus, C., 2003, Zircons from Syros, Cyclades, Greece; Recrystallization and Mobilization of Zircon During High-Pressure Metamorphism. Journal of Petrology, v. 44, no. 11, p. 1977 – 2002.

Valley, J.W., 2003, Oxygen Isotopes in Zircon. Reviews in Mineralogy and Geochemistry, 53 (1), 343-385. doi: 10.2113/0530343

Valley, J.W., Cavosie, A.J., Ushikubo, T., Reinhard, D.A., Lawrence, D.F., Larson, D.J., Clifton, P.H., Kelly, T.F., Wilde, S.A., Moser, D.E., and Spicuzza, M.J., 2014, Hadean age for a post-magma-ocean zircon confirmed by atom-probe tomography. Nat. Geosci. 7, 219–223.

Valley, J.W., Reinhard, D.A., Cavosie, A.J., Ushikubo, T., Lawrence, D.F., Larson, D.J., Kelly, T.F., Snoeyenbos, DR., and Strickland, A., 2015, Nano-and micro-geochronology in Hadean and Archean zircons by atom-probe tomography and SIMS: New tools for old minerals. American Mineralogist, v. 100, issue 7, p. 1355-1377.

Vavra, G., Gebauer, D., Schmid, R., and Compston, W., 1996, Multiple zircon growth and recrystallization during polyphase Late Carboniferous to Triassic metamorphism in granulites of the Ivrea Zone (Southern Alps): an ion microprobe (SHRIMP) study. Contributions to Mineralogy and Petrology, v. 122, p. 337-358.

Vavra, G., Schmid, R., and Gebauer, D., 1999, Internal morphology, habit and U-Th-Pb microanalysis of amphibolite-to-granulite facies zircons: geochronology of the Ivrea Zone (Southern Alps). Contributions to Mineralogy and Petrology, v. 134, p. 380-404.

Vonlanthen, P., Fitz Gerald, J. D., Rubatto, R., and Hermann, J., 2012, Recrystallization rims in zircon (Valle d'Arbedo, Switzerland): An integrated cathodoluminescence, LA-ICP-MS, SHRIMP, and TEM study. American Mineralogist, v. 97, p. 369-377.

White, L.F., Darling, J.R., Moser, D.E., Reinhard, D.A., Prosa, T.J., Bullen, D., Olson, D., Larson, D.J., Lawrence, D., and Martin, I., 2017, Atomic-scale age resolution of planetary events. Nature Communications, v.8. Article number:

15597.

Whitehouse, M.J., and Platt, J.P. (2003) Dating high-grade metamorphism—constraints from rare-earth elements in zircon and garnet. Contributions to Mineralogy and Petrology, v. 145, issue 1, p. 61-74. https://doi.org/10.1007/s00410-002-0432-z

Zeck, H.P., and Williams, I.S., 2002, Inherited and Magmatic Zircon from Neogene Hoyazo Cordierite Dacite, SE Spain—Anatectic Source Rock Provenance and Magmatic Evolution. Journal of Petrology, v. 43, no. 6, p. 1089 – 1104.

Zhang, M., Salje, E.K.H., Capitani, G.C., Leroux, H., Clark, A.M., Schlüter, J., and Ewing, R.C., 2000a, Annealing of α-decay damage in zircon: a Raman spectroscopic study. J. Phys.: Condens. Matter, v. 12, p. 3131-3148.

Zhang, M., Salje, E.K.H., Farnan, I., Graeme-Barber, A., Daniel, P., Ewing. R.C., Clark, A.M., and Leroux, H., 2000b, Metamictization of zircon: Raman spectroscopic study. J. Phys.: Condens. Matter, v. 12, p. 1915-1925.

Supplementary Materials

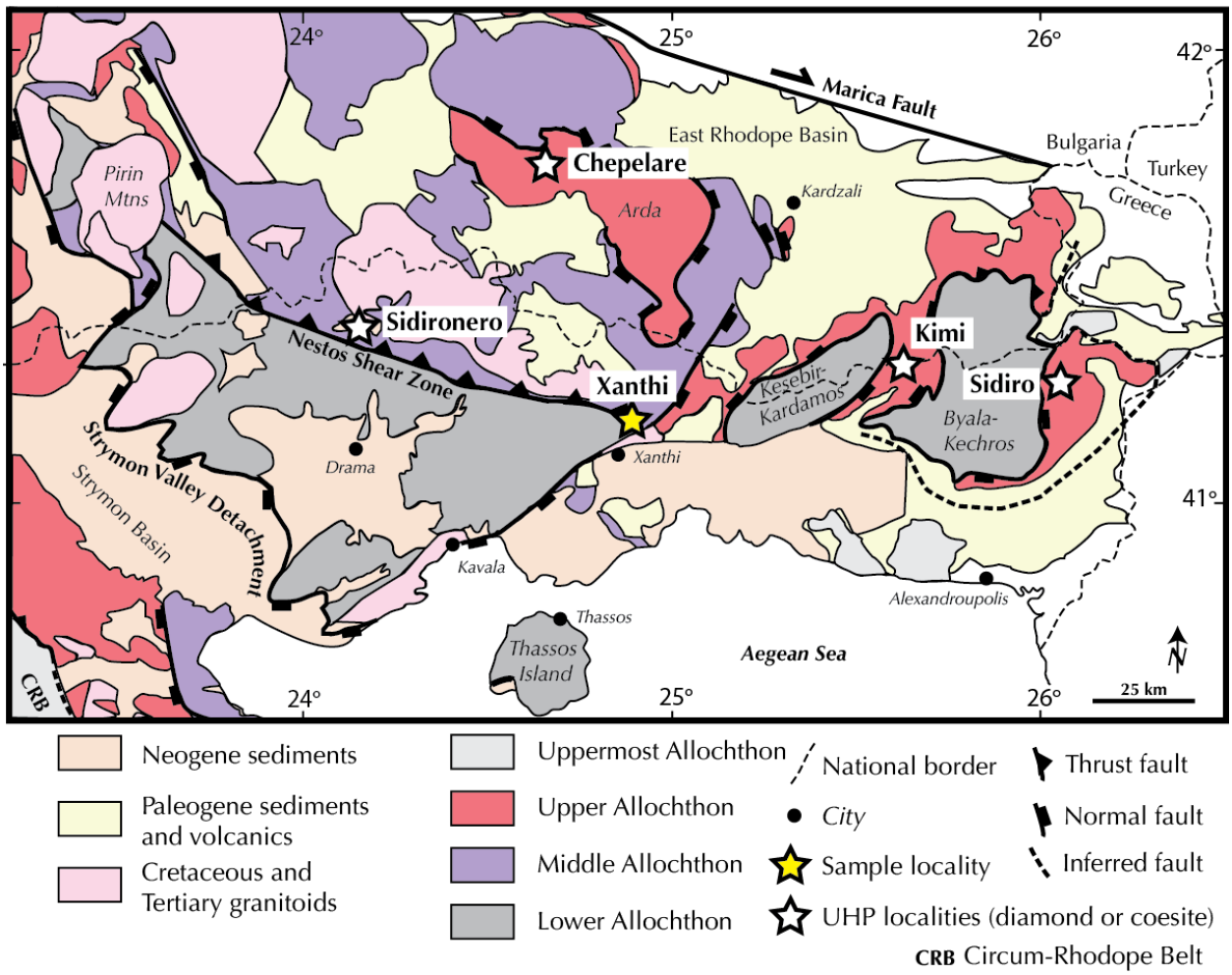

Supplemental Figure S1: Generalized geologic map of the Rhodope Metamorphic Complex (RMC), adapted from Petrík et al., 2016; Krenn et al., 2010; Janák et al., 2011. Stars mark confirmed *UHP* localities of the RMC. Sample for this study (yellow star) was collected from outcrops along the Kosynthos River, north of Xanthi. Sample coordinates: 41.18740, 24.85949.

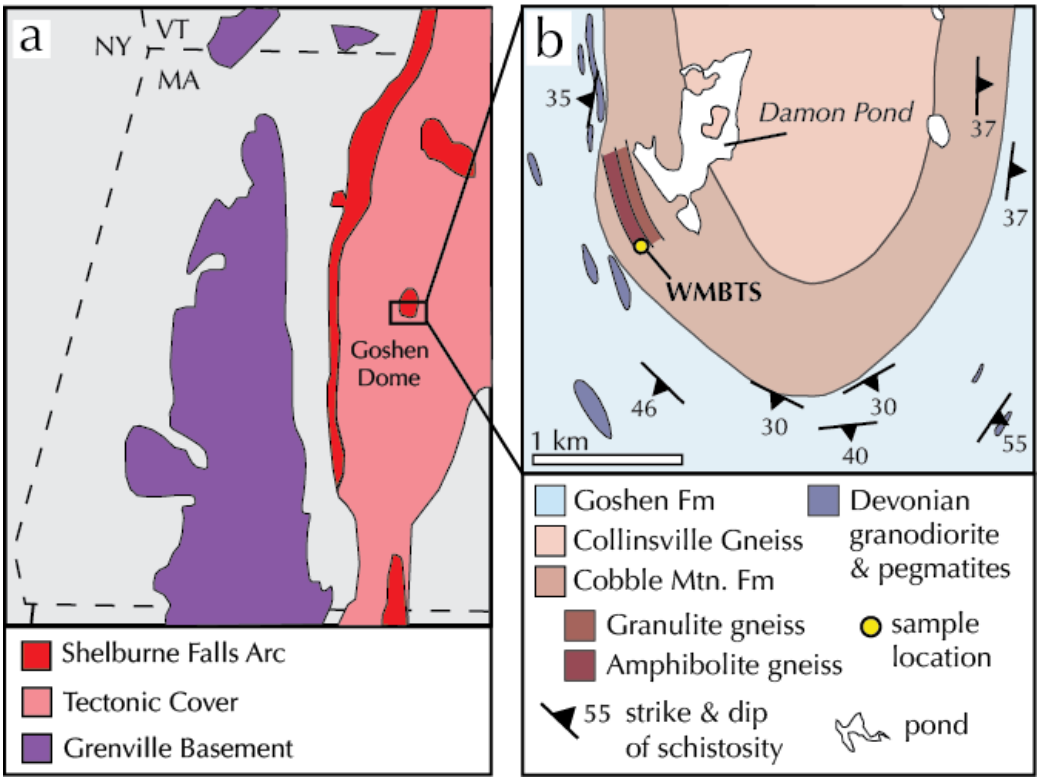

Supplemental Figure S2: Location map for sample collected from the Goshen Dome with generalized geology after Hatch and Warren (1981); figure modified after Peterman et al. (2016b). Sample was collected from the locality marked by a yellow circle within the high-grade gneisses within the Cobble Mountain Formation.

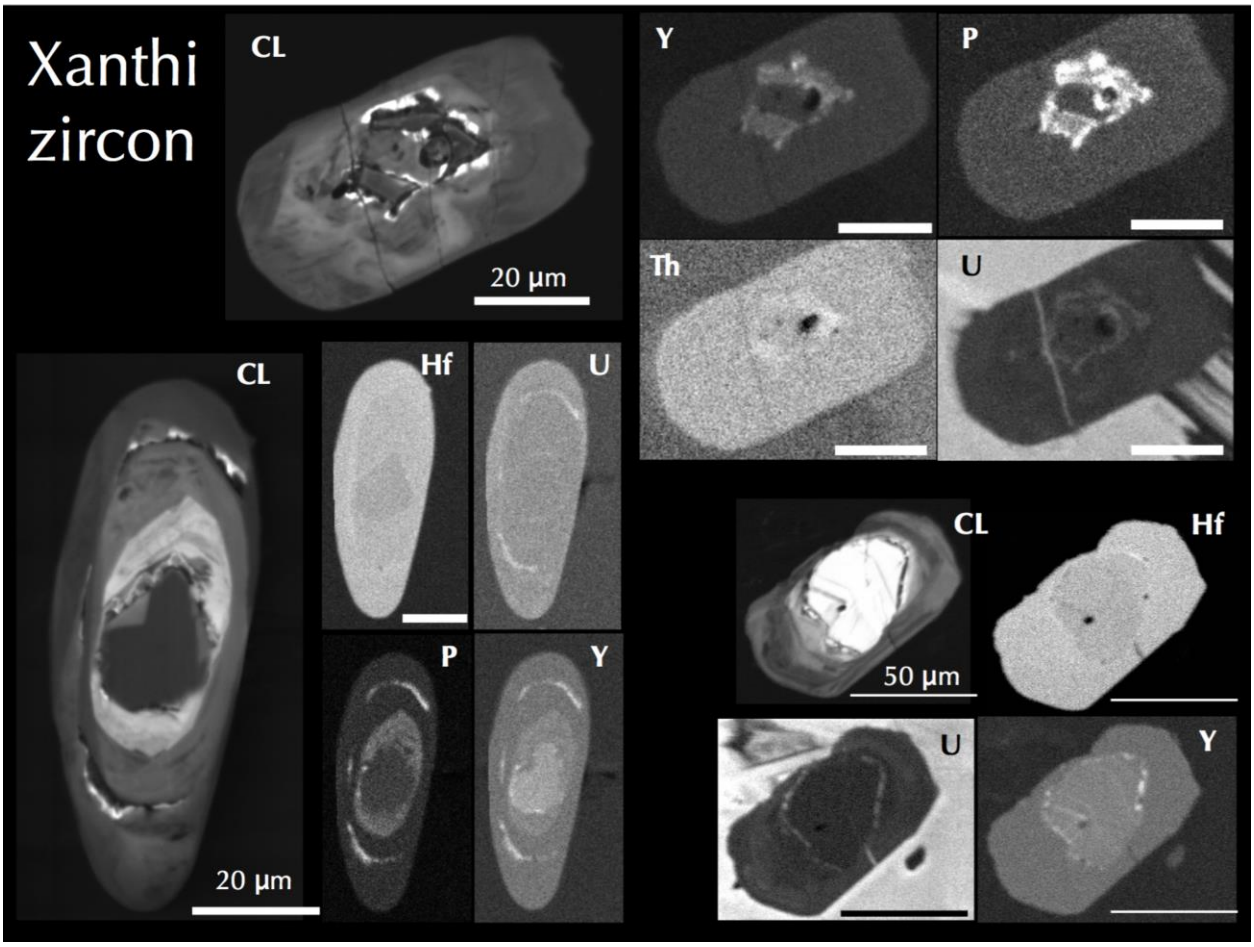

Supplemental Figure S3: Example CL images with accompanying compositional maps of three zircon grains from Rhodope. Compositional maps were collected on the CAMECA UltraChron electron microprobe at UMass, operated at 15 kV, 300 nA.

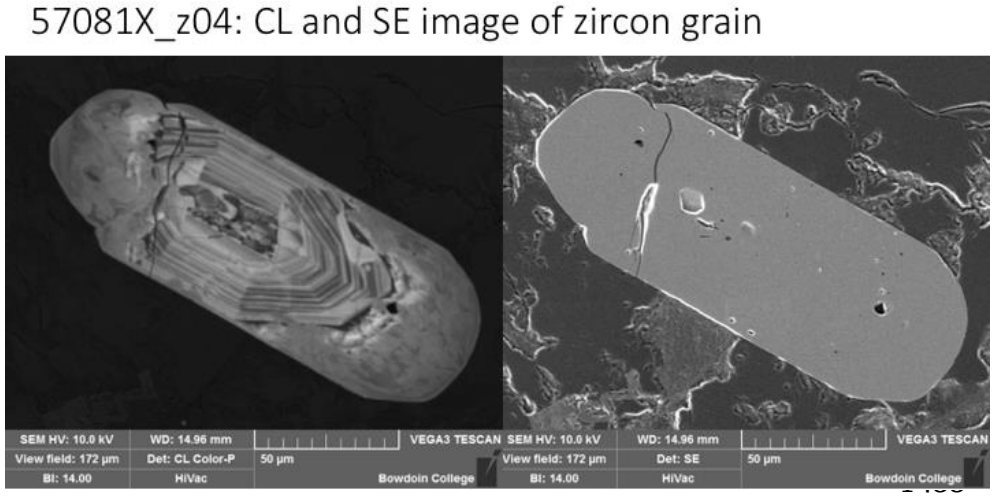

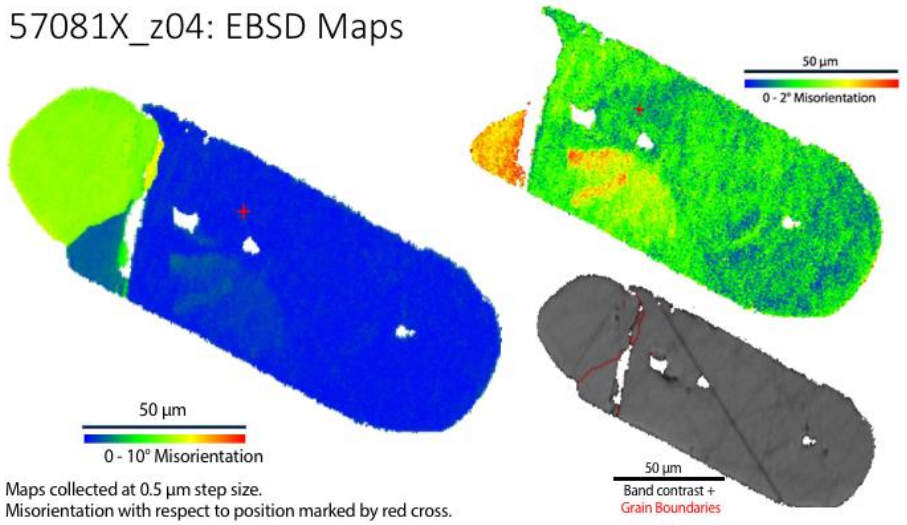

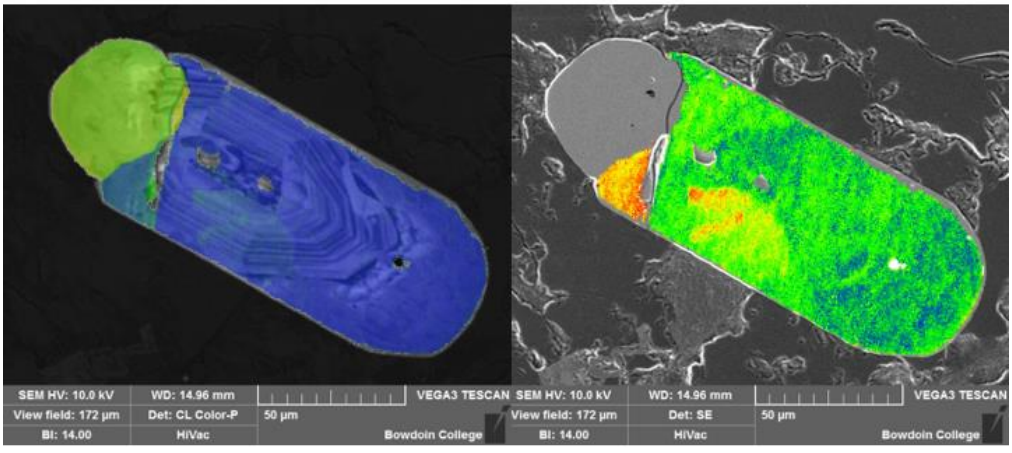

Supplemental Figure S4: SEM Images and EBSD maps of similar Rhodope zircon (57081X-z04).

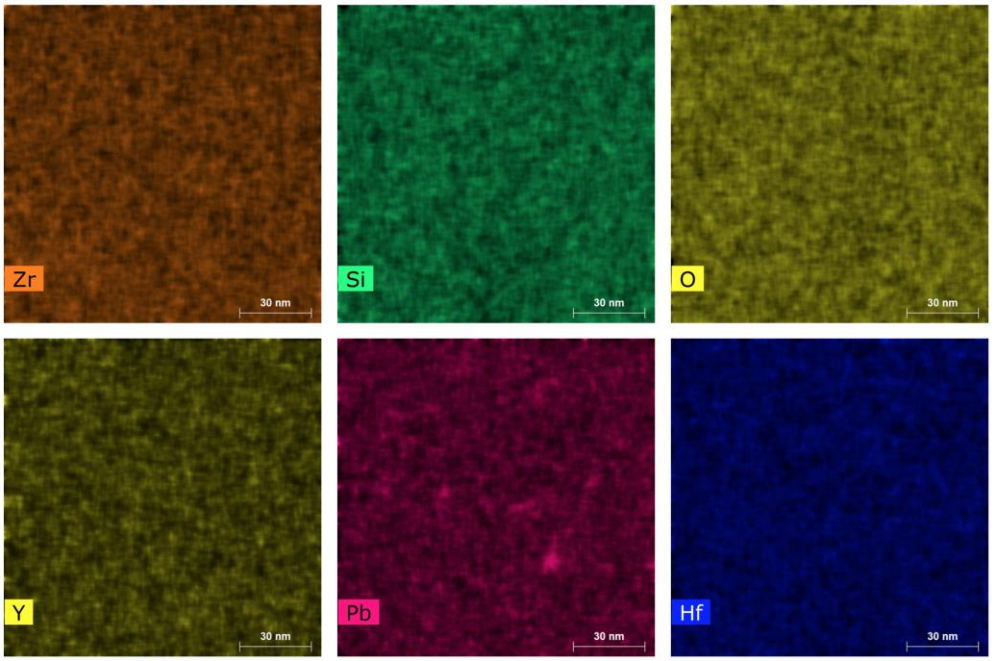

Supplemental Figure S5: Compositional maps collected from the TEM foil prepared from the Rhodope zircon analyzed in this study (grain 26).

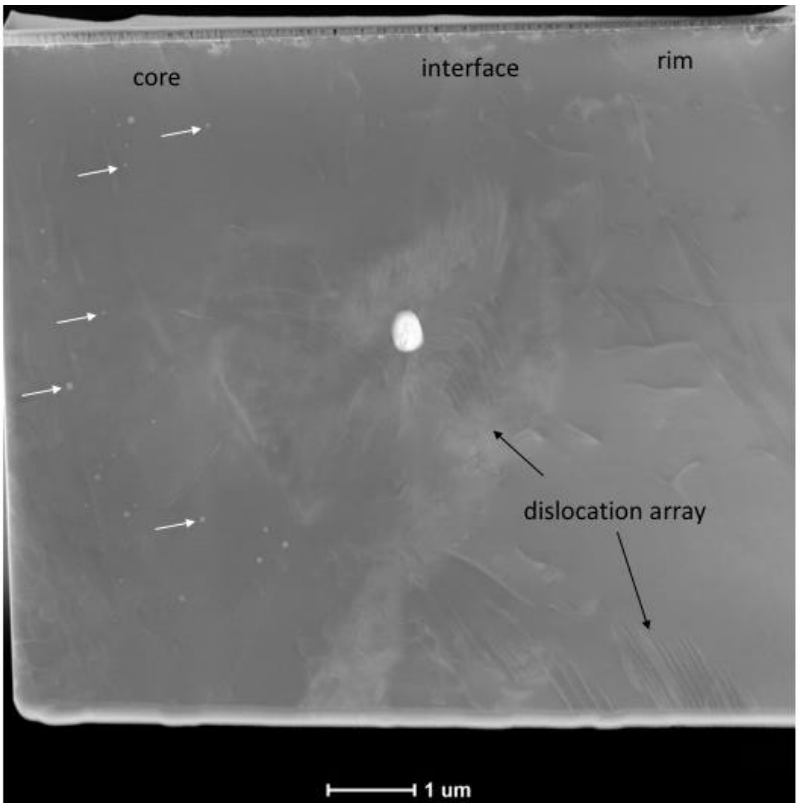

Supplemental Figure S6: STEM-DF image prepared from the Rhodope zircon analyzed in this study (grain 26). White arrows indicate bright spots (see text for discussion); black arrows indicate dislocation arrays.

Figure 1

Panchromatic CL

57074 z15

20 µm

57074-1
z13

Rainbow CL

57081X_z04

57126B
z3

Kimi

57082
z04

Rim1

Core

Rim2

Rim2

Rim1

Core1

Core2

A

Rim

LASS

LASS

LASS

LASS

Core

M17 M16 M15 M14 M13 M12

M8 M7 M6 M5 M4 M2 M1

TEM foil location

20 μm

Rim

y x

B

^{89}Y (ToF-SIMS)

M17 M16 M15 M14 M13 M12

5 μm

E

Lower hemisphere pole figure

y

{100}

{001}

x

{100}

C

Panchromatic CL

20 μm

D

BSE

20 μm

Figure 2

Figure 3

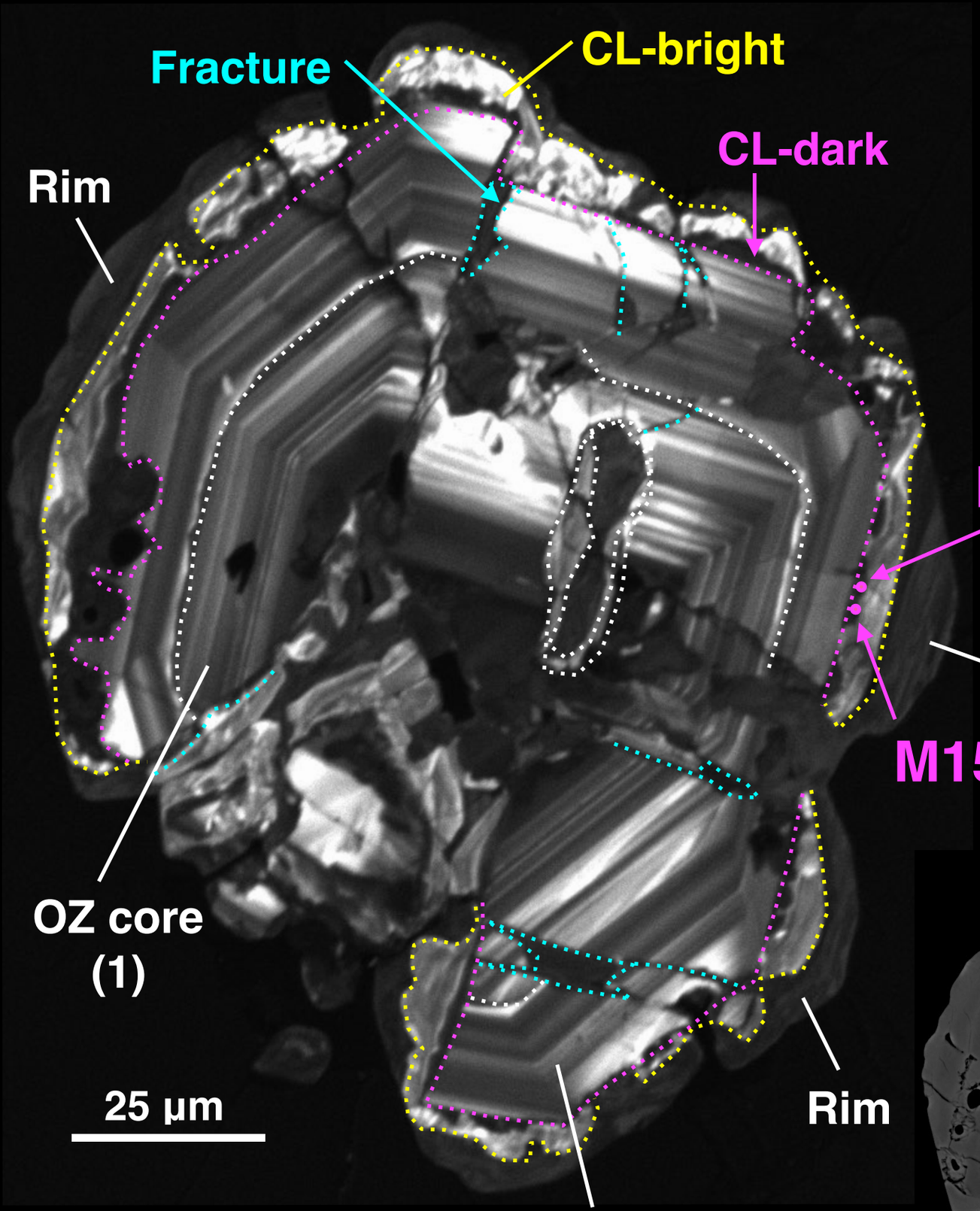

Panchromatic CL

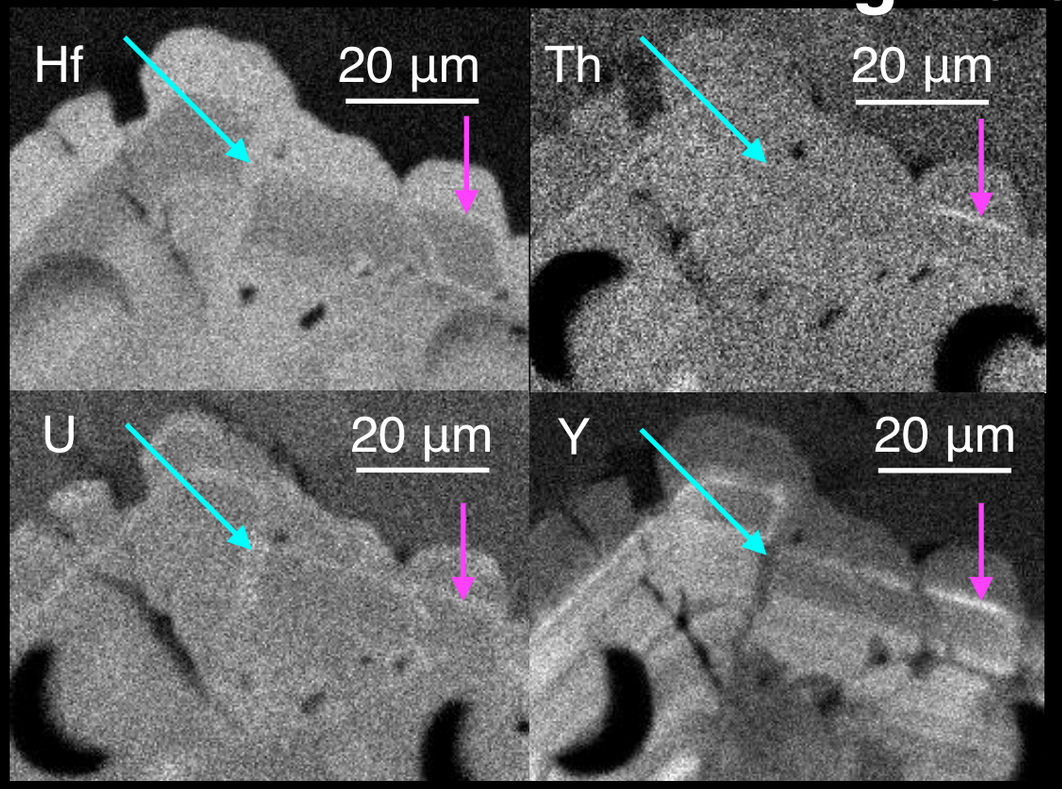

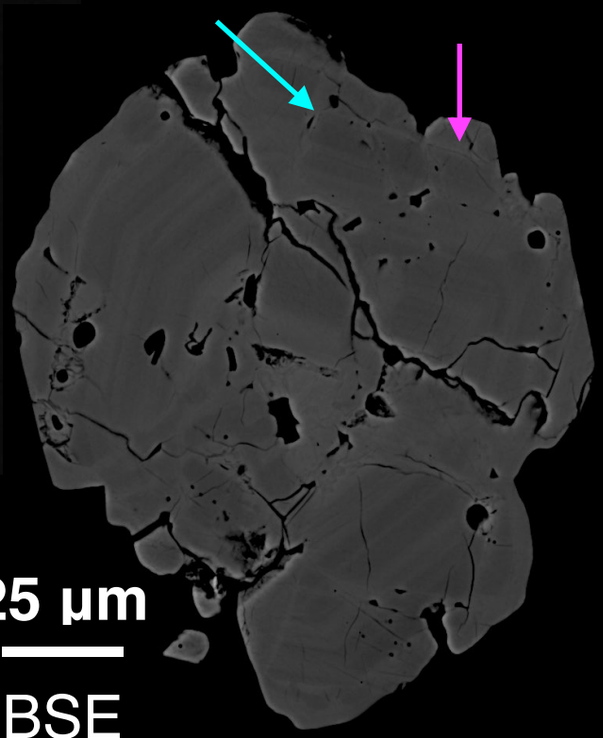

BSE

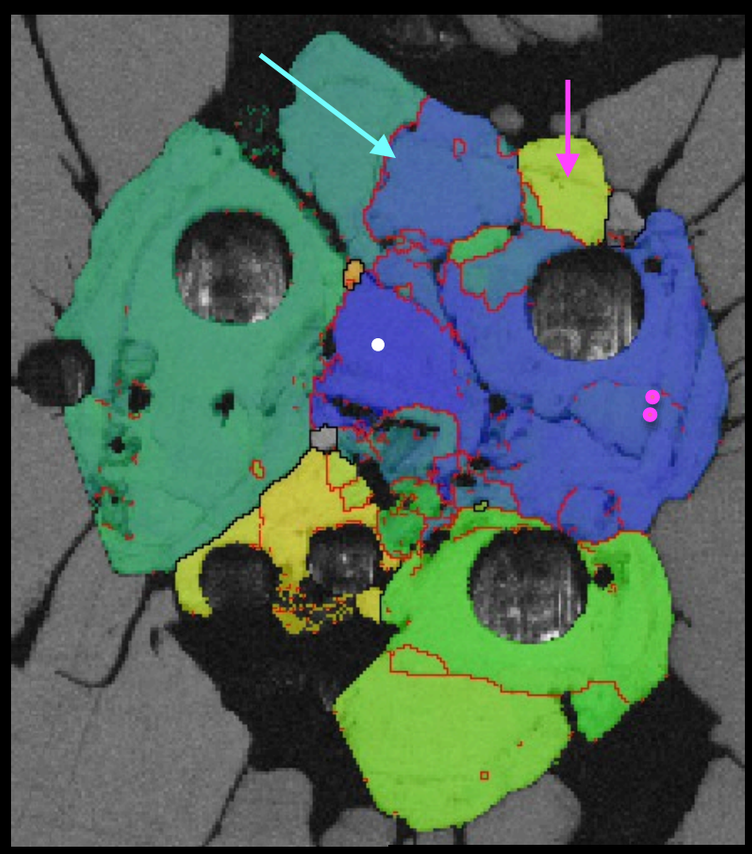

Figure 4

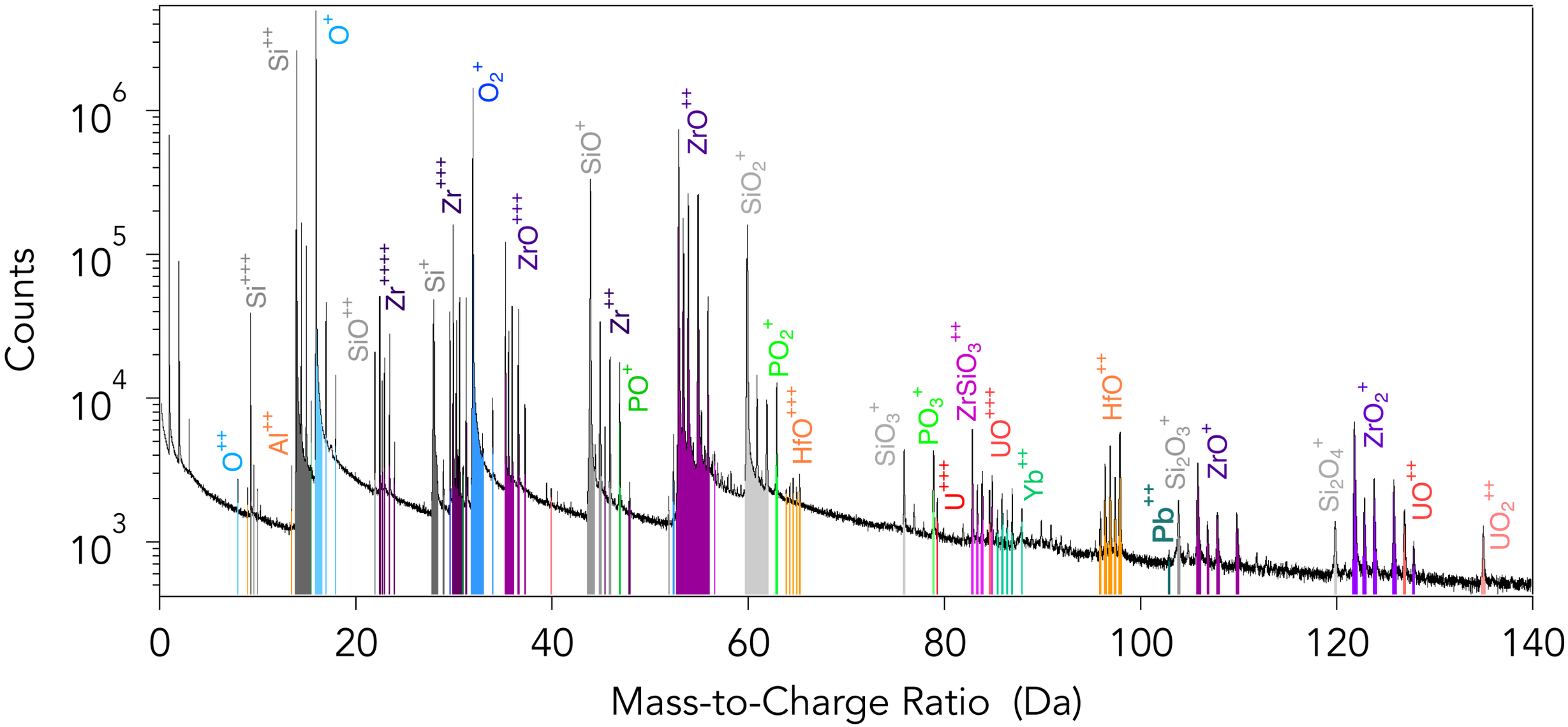
Counts
10^6
10^5
10^4
10^3
0
20
40
60
80
100
120
140
Mass-to-Charge Ratio (Da)
O++
Si+++
Si++
O+
Al++
SiO++
Zr++++
Zr+++
Si+
O2+
Zr++
PO+
ZrO+++
PO2+
HfO+++
SiO3+
PO3+
U+++
ZrSiO3++
UO+++
Yb++
SiO+
ZrO++
HfO++
Pb++
Si2O3+
ZrO+
SiO2+
Si2O4+
ZrO2+
UO++
UO2++

Figure 5

A Y + U

z-axis of specimen 100 nm

Rim (M8)

B Y + U

z-axis of specimen 100 nm

CL-bright interface (M7)

C Y + U + Pb

z-axis of specimen 100 nm

Core (M17)

D Y + Pb

z-axis of specimen 100 nm

Core (M16)

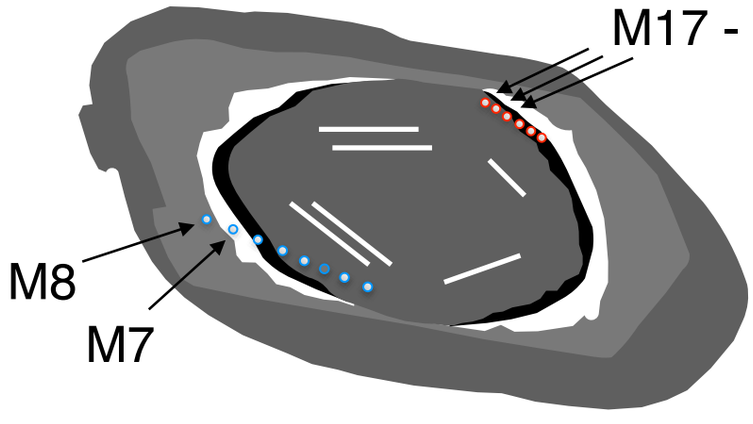

all specimens oriented:

z
x

E Y + U + Pb

z-axis of specimen 100 nm

F Y + Pb

Core (M15)

Figure 6

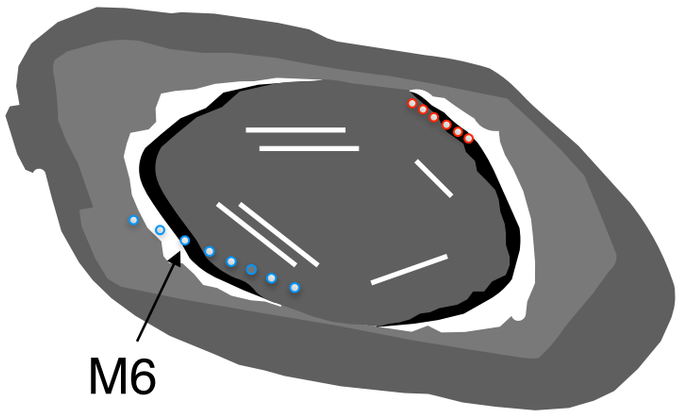
M6

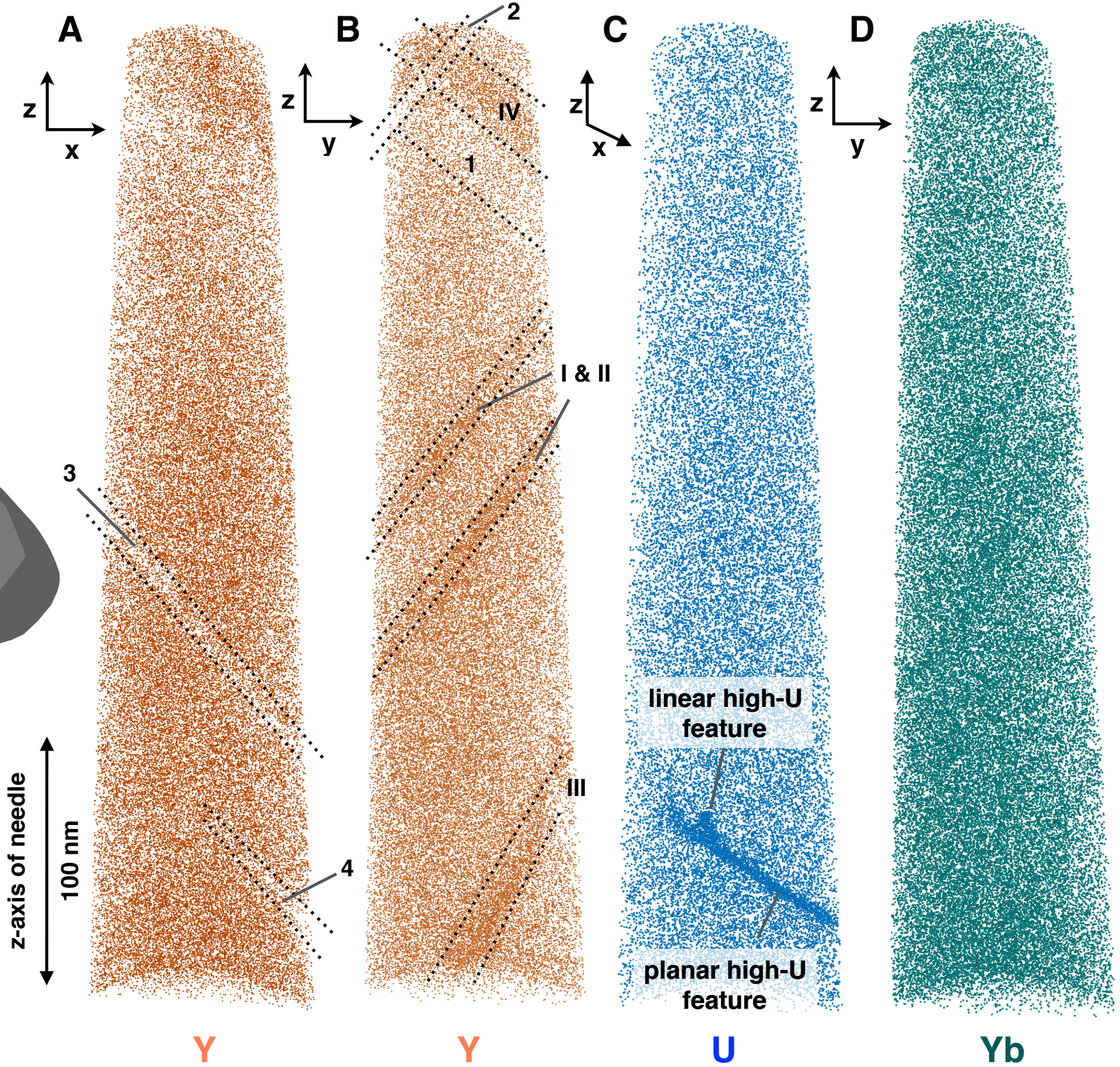
A
B
C
D
z
x
y
z
y
z
x
z
y
2
IV
1
I & II
3
III
4
z-axis of needle
100 nm
linear high-U feature
planar high-U feature
Y
Y
U
Yb

Figure 7

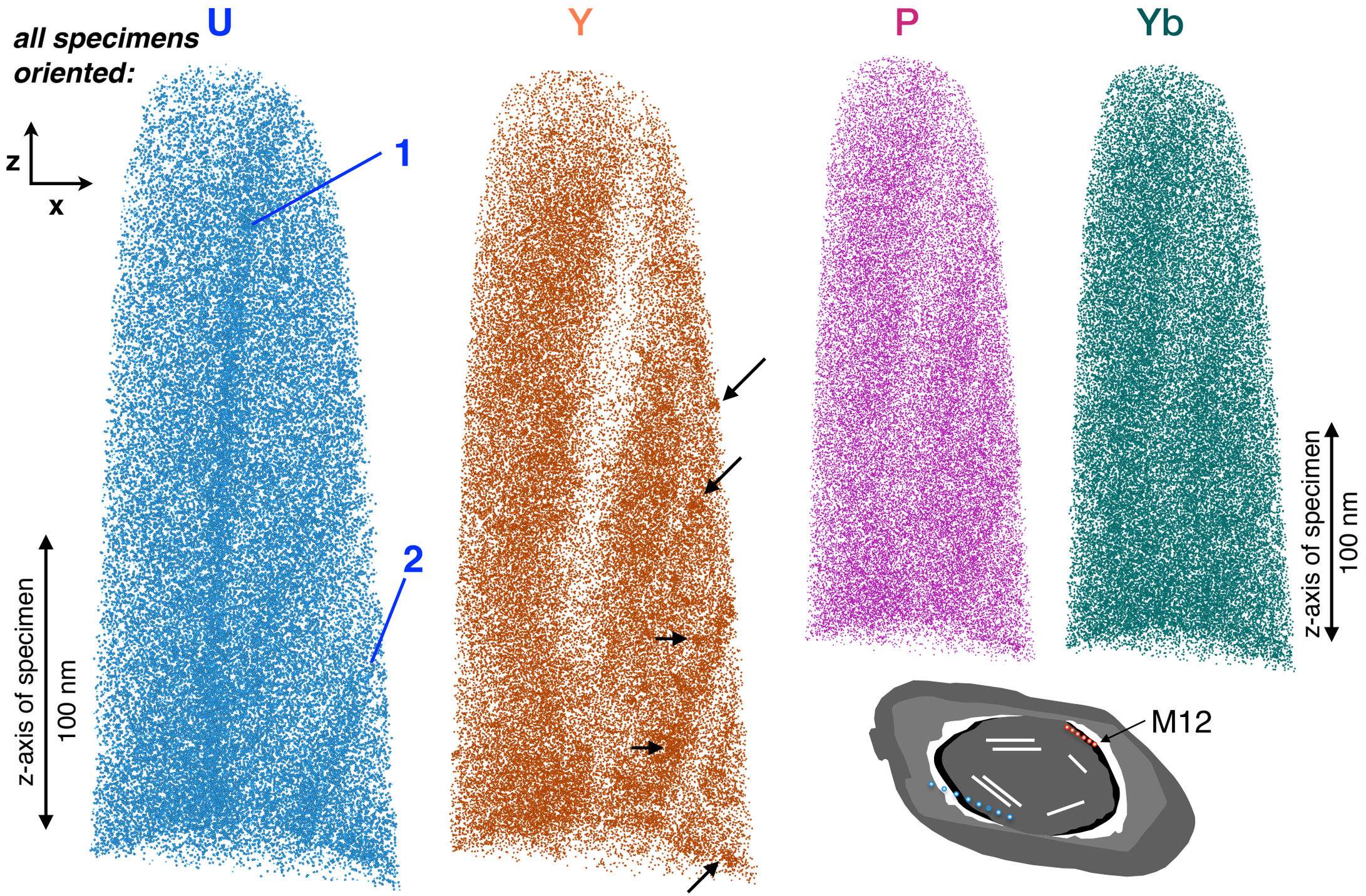
all specimens oriented:
z
x
U
1
2
z-axis of specimen
100 nm
Y
P
Yb
z-axis of specimen
100 nm
M12

Figure 8

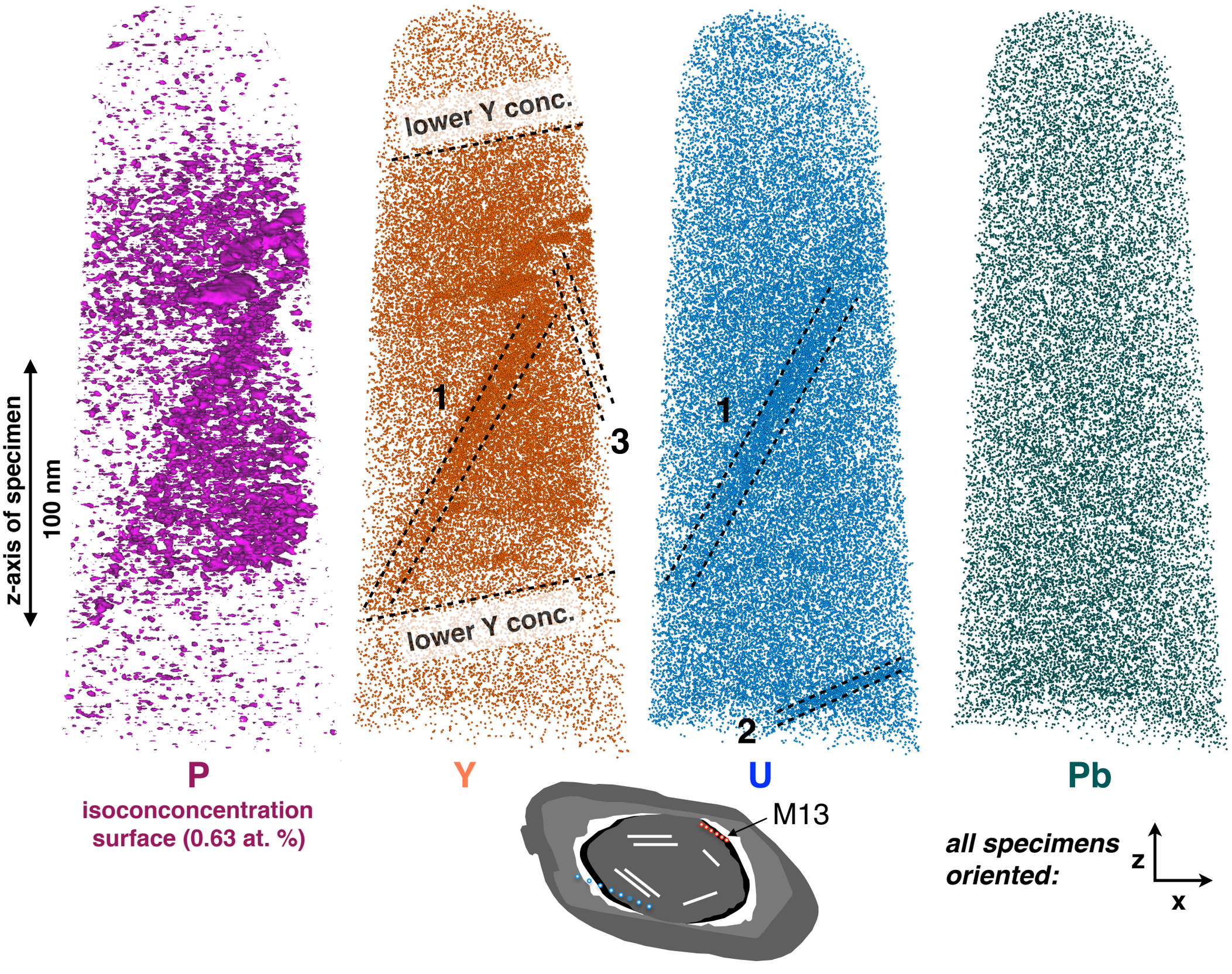
z-axis of specimen
100 nm
lower Y conc.
1
3
lower Y conc.
1
2
P
isoconconcentration surface (0.63 at. %)
Y
U
Pb
M13
all specimens oriented:
z
x

U + Y + PO_3 + Al + Yb + Pb

U

Y

PO_3

Yb

Al

Pb

z-axis of specimen

100 nm

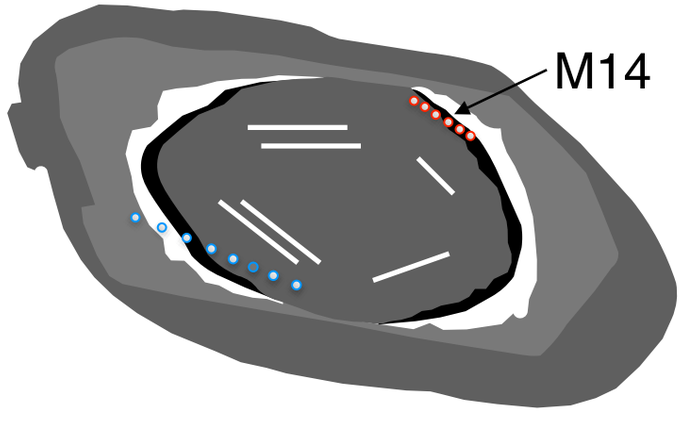

all specimens oriented: z x

Figure 9

Figure 10

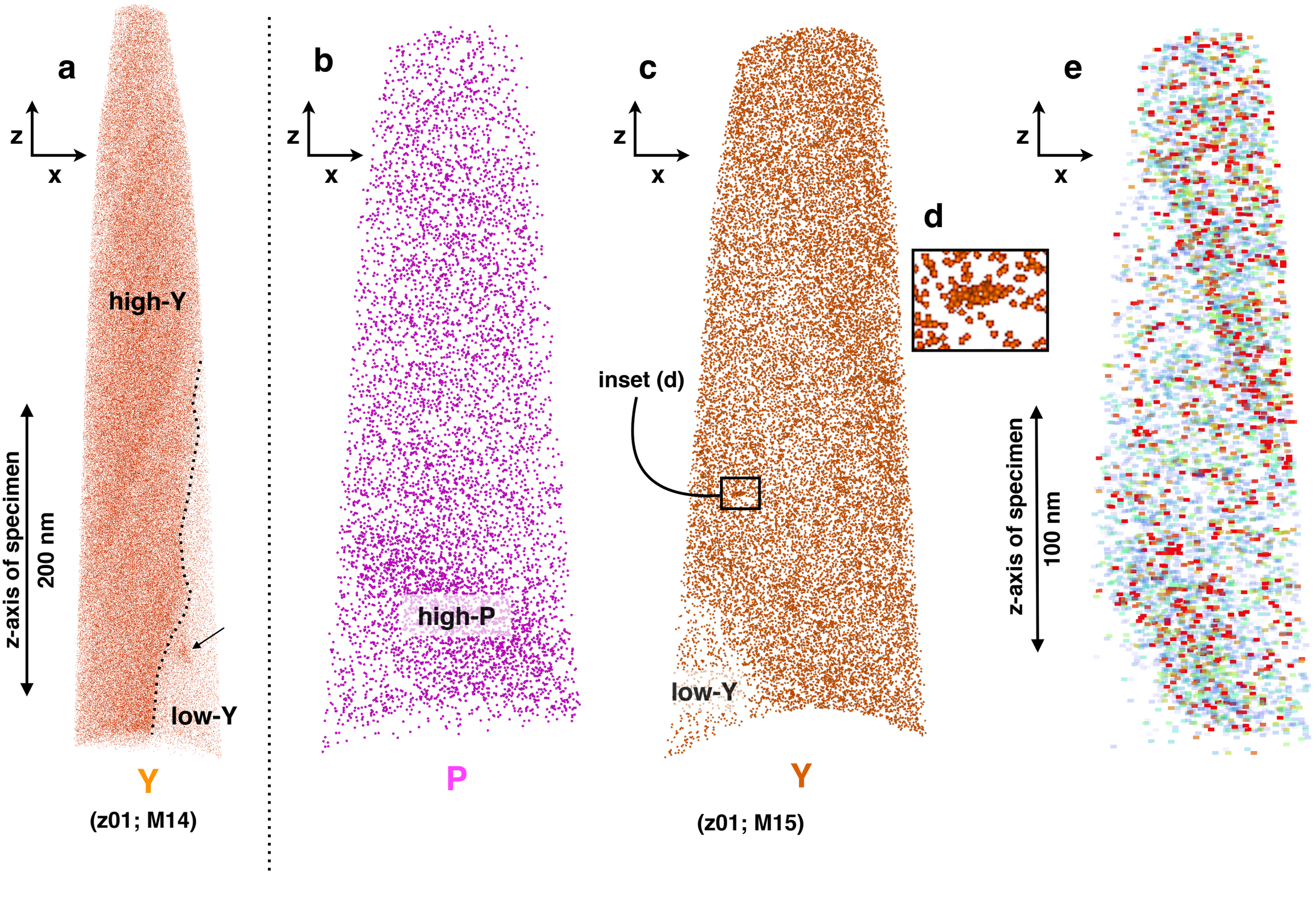
a
z
x
high-Y
z-axis of specimen
200 nm
low-Y
Y
(z01; M14)
b
z
x
high-P
P
c
z
x
inset (d)
low-Y
Y
(z01; M15)
d
e
z
x
z-axis of specimen
100 nm

Figure 11

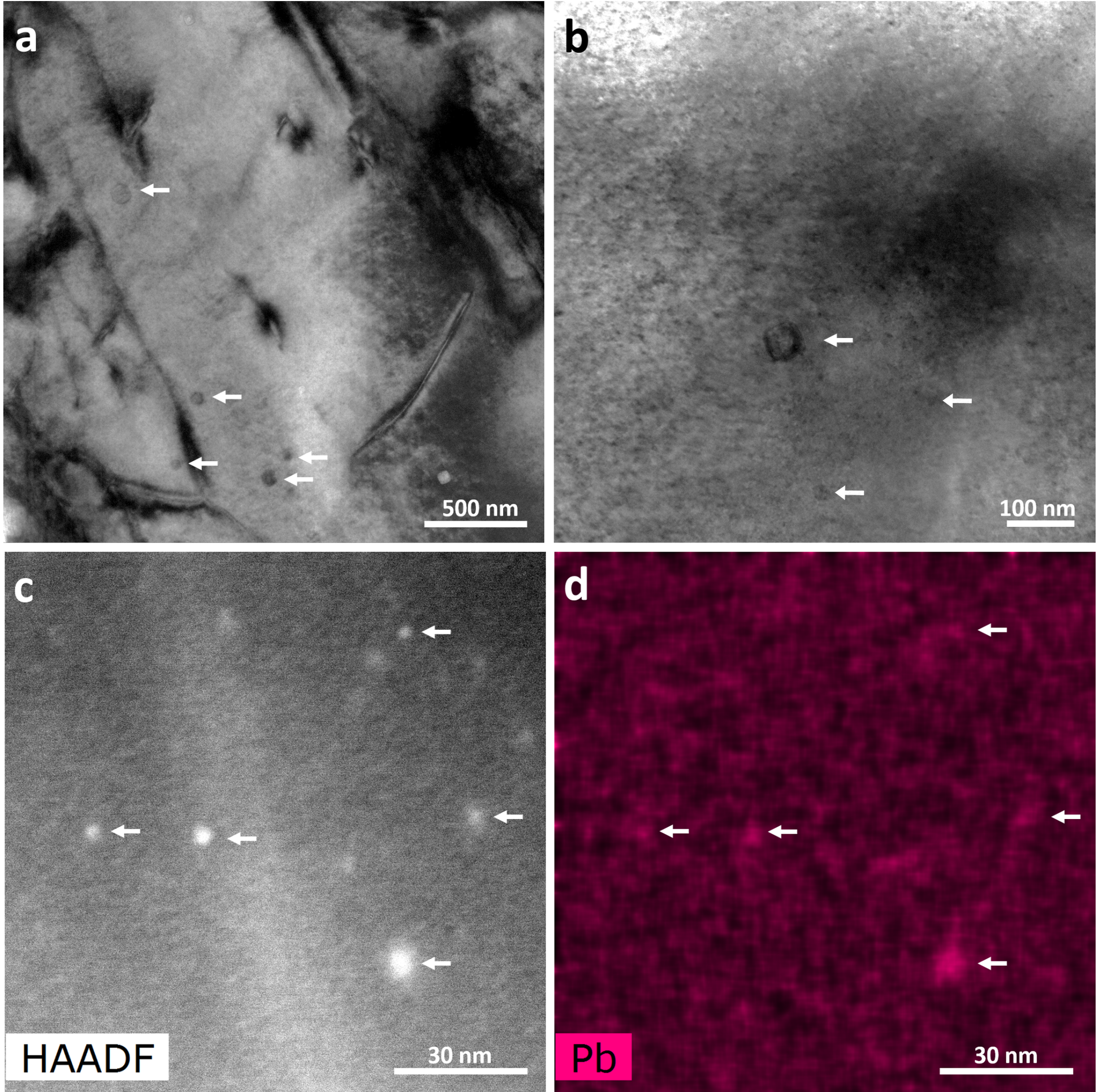

Figure 12

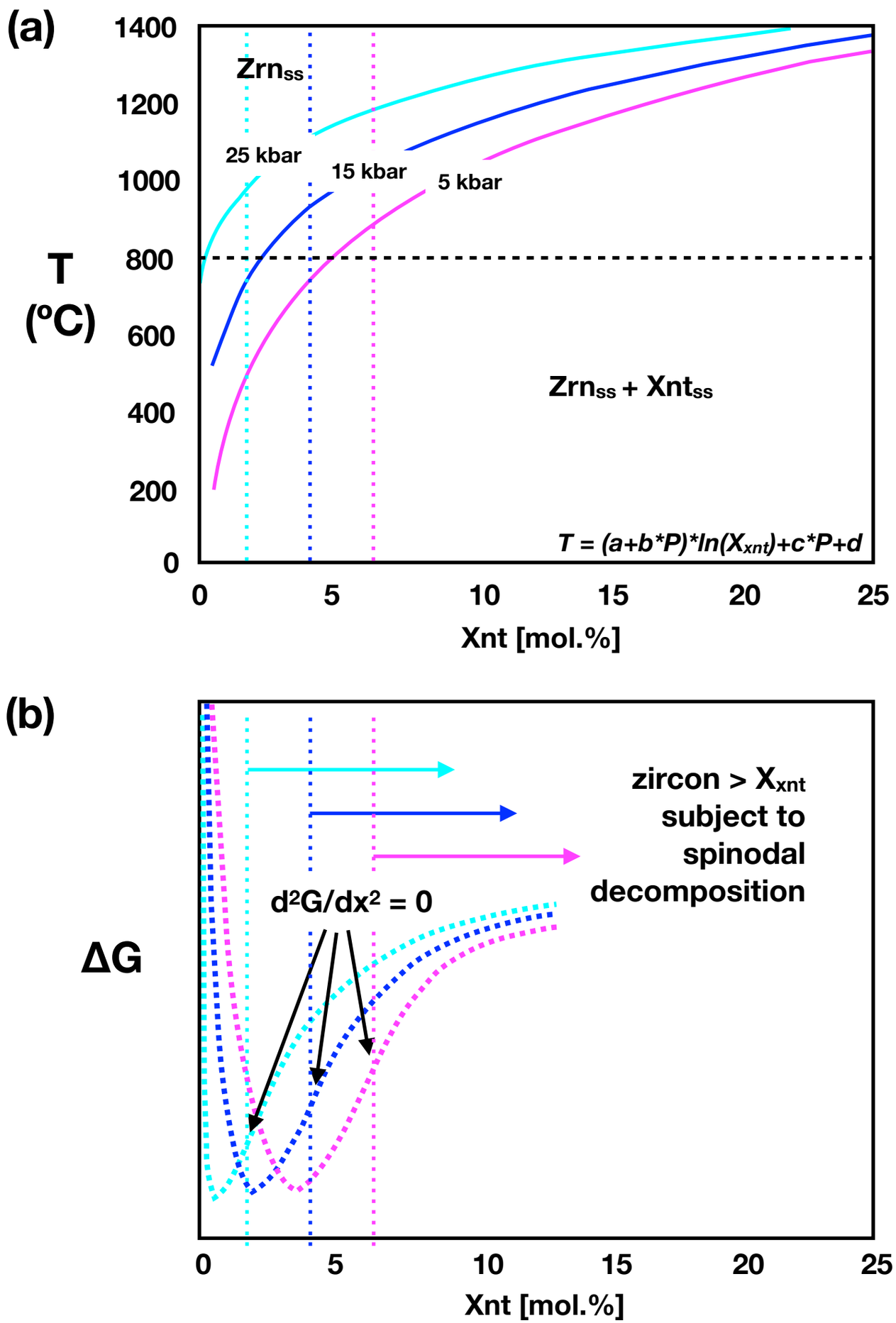
(a)
T (ºC)
1400
1200
1000
800
600
400
200
0
Zrn$_{ss}$
25 kbar
15 kbar
5 kbar
Zrn$_{ss}$ + Xnt$_{ss}$
$T = (a+b*P)*ln(X_{xnt})+c*P+d$
0
5
10
15
20
25
Xnt [mol.%]
(b)
ΔG
zircon > X_{xnt} subject to spinodal decomposition
$d^2G/dx^2 = 0$
0
5
10
15
20
25
Xnt [mol.%]

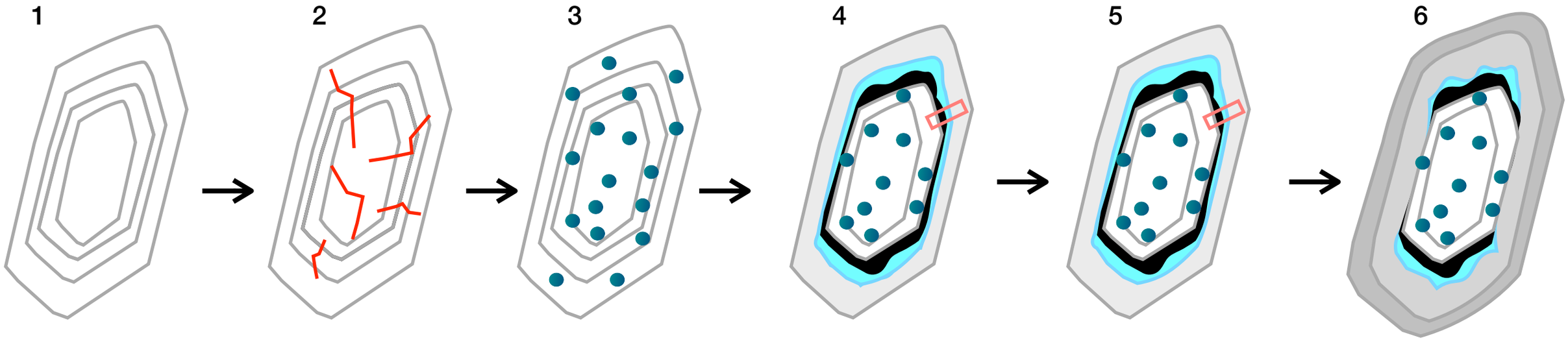

Crystallization (c. 2.14 Ga)

Accumulate radiation damage

Prograde metm. anneals radiation damage; forms dislocation loops that filll with Pb prior to 150 Ma

ICDR front forms interface domain; U + Y + P + REE accumulate along front & form planar features; decorate dislocations

Spinodal decomposition produces ellipsoidal features within planar features

c. 150 Ma rim recrystallizes at garnet-stable conditions; may locally overprint interface domain (I.D.)

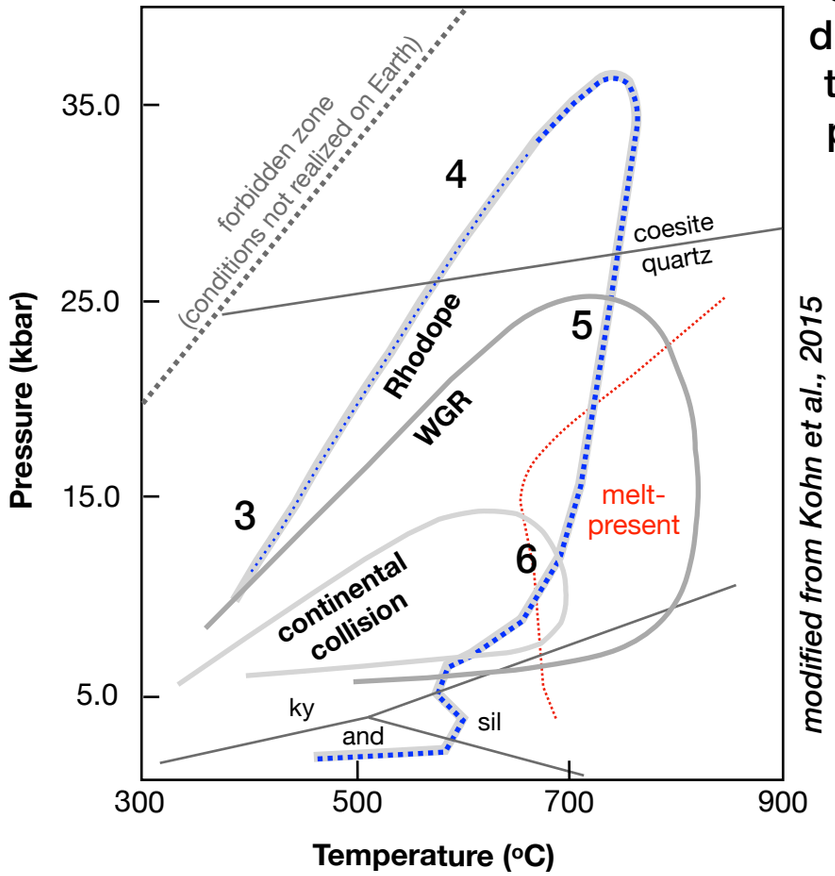

modified from Kohn et al., 2015

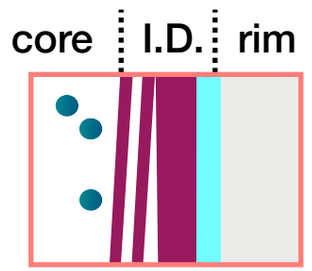

schematic cross-section through zircon domains

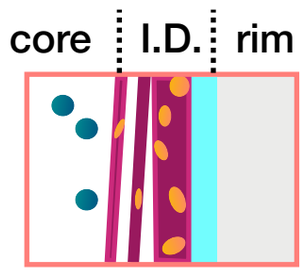

schematic cross-section through zircon domains

Symbols:

- Radiation damage
- Pb clusters
- CL-dark domain
- planar features
- CL-bright domain
- reacted zircon
- ellipsoidal feature
- zircon rim

Table 2 – Nanoscale features observed via Atom Probe Tomography

Feature type	Toroidal cluster	Planar feature	Ellipsoidal cluster	Linear feature
Chemical attributes[1] (ppma or at. %)	High Pb (+Y, +Al) Pb: 2.0–5.5 at. % Y, Al: 0–1.0 at. %[2]	1) High Y, P, Yb 1100–3300 ppma, 150–790 ppma, 180–535 ppma 2) Low Y, P, Yb 0–430 ppma, 30–140 ppma, 120–235 ppma 3) High U 2000–2900 ppma 4) Low U 183 ± 12 ppma	High Y, P, Yb, (+ Al) 10500 – 19000 ppma Y 2800 – 5600 ppma P 1750 – 2630 ppma Yb 31 ppma Al Up to 160 ppma Pb with high variability among specimens	High U (>5000 ppma) + Al (1660 ppma) High Y (1445 ± 67 ppma) + Yb (280 ± 29 ppma)
Morphology	Toroidal	Dominantly planar; some curviplanar	Clumps; no discernible hole	Linear
Scale	<20 nm diameter; some <10 nm	20 to 50 nm thick; some >100 nm	10 to 50 nm diameter	<10 nm in diameter; 30 nm long
Factor of enrichment (compared with bulk needle composition)	Pb: below background in specimen	1) Y: 1.25–1.65; P: 1.4–1.7; Yb: 1.38–1.85 2) Y: 0.0–0.32; P: 0.19–0.62; Yb: 0.33–0.89 3) U: 5–16 4) U: 0.39	Y: 6.5–28 P: 6.7–25 Yb: 5.7 – 14	U: > 30, Al: below background in specimen Y: 3.38, Yb: 4.6 compared with low-Y planar host

[1] Concentrations given as range; measured values and uncertainties reported in Table 3.

[2] Peterman et al., 2016a

Table 3

Click here to access/download;Table;Table 3 - APT compositional data.xlsx

	M17		M15		M
at%	Whole		Whole		Wh
Si	17.37	0.01	17.34	0.01	17.27
Zr	18.23	0.01	18.06	0.01	18.16
O	63.14	0.02	63.18	0.02	63.97
ppma					
Y	94	2	92	2	47
Ti	64	2	69	1	62
P	69	2	55	1	35
Yb	53	1	47	1	11
U	71	2	71	1	34
Pb	20	1	14	1	-
Al	-	-	-	-	-
Hf	1950	9	1961	7	1319

Uncertainties reported at 1σ

- denotes below detection

I8		M7				M6	
ole		Whole		Whole		U-rich planar	
	0.01	17.00	0.01	17.05	0.01	16.85	0.05
	0.01	17.68	0.01	17.99	0.01	17.37	0.05
	0.02	62.48	0.02	62.81	0.01	62.94	0.12
	1	17	1	1079	4	646	30
	1	74	1	64	1	86	11
	1	51	1	377	3	177	16
	1	30	1	403	3	278	20
	1	49	1	176	2	2886	63
-		-	-	-	-	-	-
-		-	-	-	-	203	17
	6	2026	7	2076	6	2205	55

												M
U-rich linear			Whole			Y-low planar			U-rich			
16.39	0.21		17.08	0.01		17.20	0.03		16.92			
16.93	0.22		17.93	0.01		18.04	0.03		17.72			
63.03	0.50		63.22	0.01		63.30	0.07		63.42			
1871	212		1285	5		165	9		1244			
77	43		63	1		53	5		86			
205	70		385	3		72	6		287			
407	99		294	3		120	8		325			
5940	379		473	3		526	16		2559			
-	-		-	-		-	-		59			
1660	200		-	-		-	-		-			
1651	199		2033	7		2147	33		1889			

12						
planar	U-poor		Y-rich Ellipsoidal Clusters		Whole	
0.07	17.27	0.04	15.69	0.11	17.20	0.01
0.07	18.30	0.04	17.64	0.12	17.97	0.01
0.15	63.91	0.09	63.43	0.27	63.13	0.01
53	1801	37	10573	274	691	4
14	41	6	60	21	71	1
26	588	21	2802	141	226	2
27	370	17	1763	112	185	2
77	183	12	491	59	281	2
12	-	-	114	28	-	-
-	-	-	-	-	-	-
66	2174	41	2551	134	1982	6

M13						
Y low (Top)		Y high (Top)		U-rich planar		Y-rich Ellipso
17.39	0.03	17.18	0.03	16.97	0.05	14.65
18.21	0.03	18.09	0.03	17.50	0.05	18.22
63.30	0.07	63.36	0.07	63.54	0.12	63.07
222	10	1089	24	2039	52	19015
93	6	66	6	86	11	37
140	8	387	14	579	28	5587
166	8	342	13	483	25	2633
81	6	275	12	1972	52	486
-	-	-	-	-	-	161
-	-	-	-	-	-	-
2248	31	2065	33	1891	50	2102

						M14	
idal Clusters	Whole		Y-low		Y-rich		
0.16	17.02	0.01	17.32	0.05	17.18	0.03	
0.18	17.89	0.01	18.18	0.05	17.66	0.03	
0.40	63.06	0.01	63.26	0.11	63.38	0.07	
543	1978	6	0	0	3273	40	
24	64	1	92	10	57	5	
293	538	3	140	12	789	20	
201	389	2	233	16	535	16	
86	454	3	529	24	392	14	
49	-	-	-	-	-	-	
-	30	1	22	5	28	4	
179	53	1	2386	51	2206	33	

U-rich		Y-rich Ellipsoidal Clusters		
16.80	0.10	15.72	0.02	at% Si
17.90	0.10	17.33	0.02	Zr
63.29	0.23	63.27	0.05	O
				ppma
1715	94	12948	62	Y
42	15	59	4	Ti
335	41	3599	33	P
362	43	2228	26	Yb
2910	122	766	15	U
61	18	157	7	Pb
-	-	31	3	Al
2438	112	1981	24	Hf

M14 - Goshen Dome							
Whole		Y-low planar		Y-rich planar		Y-rich	
17.11	0.00	17.02	0.03	17.44	0.03	17.48	
17.65	0.00	17.22	0.03	17.84	0.03	18.22	
62.13	0.01	61.83	0.07	62.47	0.06	63.96	
1942	5	427	15	2458	30	1445	
58	1	68	6	49	4	99	
138	1	54	5	193	8	84	
183	1	61	6	258	10	280	
44	1	-	-	38	4	-	
-	-	-	-	-	-	-	
-	-	-	-	-	-	-	
1157	4	1499	29	1178	21	1451	

	M15 - Goshen Dome					
linear	Whole		Y-low planar		Y-rich planar	
0.08	17.32	0.01	17.17	0.03	17.33	0.01
0.08	18.20	0.01	18.00	0.04	18.21	0.01
0.18	62.77	0.01	62.64	0.08	62.78	0.01
67	2077	7	299	13	2142	7
17	58	1	50	5	58	1
16	143	2	31	4	148	2
29	175	2	77	7	180	2
-	56	1	-	-	59	1
-	-	-	-	-	-	-
-	-	-	-	-	-	-
67	1174	5	1470	30	1164	5